International Journal of Thermophysics (2024) 45:156
https://doi.org/10.1007/s10765-024-03449-6

Thermophysical Properties of the Hydrogen Carrier System Based on Aqueous Solutions of Isopropanol or Acetone

Thomas M. Koller[1] · Julius H. Jander[1] · Chathura J. Kankanamge[1] · Lena M. Braun[1] · Pranay K. Chittem[1] · Manuel Kerscher[1] · Michael H. Rausch[1] · Tobias Klein[1] · Peter Wasserscheid[2,3,4] · Andreas P. Fröba[1]

Received: 8 October 2024 / Accepted: 15 October 2024 / Published online: 1 November 2024

Abstract

One concept for the safe storage and transport of molecular hydrogen (H_2) is the use of hydrogen carrier systems which can bind and release hydrogen in repeating cycles. In this context, the liquid system based on isopropanol and its dehydrogenated counterpart acetone is particularly interesting for applications in direct isopropanol fuel cells that are operated with an excess of water. For a comprehensive characterization of diluted aqueous solutions of isopropanol or acetone with technically relevant solute amount fractions between 0.02 and 0.08, their liquid density, liquid viscosity, and interfacial tension were investigated using various light scattering and conventional techniques as well as equilibrium molecular dynamics (EMD) simulations between (283 and 403) K. Polarization-difference Raman spectroscopy (PDRS) was used to monitor the liquid-phase composition during surface light scattering (SLS) experiments on viscosity and interfacial tension. For comparison purposes and to expand the database, capillary viscometry and dynamic light scattering (DLS) from bulk fluids with dispersed particles were also applied to determine the viscosity while the pendant-drop (PD) method allowed access to the interfacial tension. By adding isopropanol or acetone to water, density and, in particular, interfacial tension decrease significantly, while viscosity shows a pronounced increase. The behavior of viscosity and interfacial tension is closely related to the strong hydrogen bonding between the unlike mixture components and the pronounced enrichment of both solutes at the vapor–liquid interface, as revealed by EMD simulations. For an aqueous solution with an isopropanol amount fraction of 0.04, minor variations in interfacial tension and viscosity were found in the presence of pressurized H_2 up to 7.5 MPa. Overall, the results from this study contribute to an extended database for diluted aqueous solutions of isopropanol or acetone, especially at temperatures above 323 K.

Keywords Acetone · Aqueous solutions · Direct fuel cell · Hydrogen carrier system · Isopropanol · Thermophysical properties

Extended author information available on the last page of the article

1 Introduction

The storage and transport of green hydrogen (H_2) obtained by hydrolysis using renewable energy sources is one important step in the transformation of the global energy system. At present, different corresponding concepts are discussed for large-scale applications. In its pure form, H_2 can be compressed in the gaseous state at pressures up to 75 MPa [1–3] or liquefied at temperatures down to 20 K [4, 5]. Alternatively, H_2 can be physically or chemically bound to other substances for storage. Physical storage can be realized by adsorption to metal organic frameworks [6], zeolites [7], or carbon nanotubes [8]. Examples for chemically bound hydrogen are its storage in metal hydrides [9], its reaction with carbon monoxide (CO) or carbon dioxide (CO_2) to methanol or other organic molecules [10, 11], or the reversible hydrogenation of liquid organic hydrogen carriers (LOHCs) [12–14]. The latter are organic and, in most cases, aromatic molecules that chemically bind H_2 by catalytic hydrogenation, while H_2 is released by catalytic dehydrogenation. In both the unloaded dehydrogenated and the loaded hydrogenated state, LOHCs are in the liquid state, which allows the safe storage and transportation of H_2 using the existing infrastructure established for liquid fuels. In recent and ongoing research activities, homocyclic hydrocarbon-based molecules, such as benzyltoluene and dibenzyltoluene or their mixtures, were found to be promising LOHC compounds with relatively high energy densities [12, 15, 16].

During the highly endothermic dehydrogenation of aliphatic hydrocarbon LOHC compounds, reaction temperatures above 523 K are typically required. This energy-demanding process step can lower the energetic efficiency of the LOHC system if no waste heat from other processes is available [13, 14, 16, 17]. To improve efficiency, one approach is to replace the dehydrogenation step by a transfer hydrogenation. Here, the hydrogenated LOHC molecule, e.g., perhydrobenzyltoluene, is dehydrogenated by transferring two hydrogen atoms to an acceptor molecule like acetone that is hydrogenated to isopropanol [17–19]. The advantage is that this reaction takes place at considerably lower temperatures typically below 473 K and, most importantly, is nearly thermoneutral [19]. However, the acetone/isopropanol system, which can also be viewed as an LOHC system, features lower H_2 storage capacities compared to the aforementioned LOHC systems. Nevertheless, the isopropanol/acetone system is particularly interesting for applications in direct fuel cells (DFCs).

In DFCs, the hydrogenated isopropanol can be used to produce electricity on demand without the necessity to handle molecular H_2. At the anode of the DFC, isopropanol is oxidized to acetone by releasing electrons and protons (H^+). The latter are transferred from the anode through a membrane to the cathode, where they react with oxygen (O_2) from air to form water. The oxidation product acetone can be reloaded with H_2 by a subsequent hydrogenation to isopropanol in energy-rich states where hydrogen production through electrolysis is beneficial. Such so-called "isopropanol DFCs" are in the focus of current research activities [19–24] because secondary alcohols like isopropanol show some very interesting features compared to other alcohols like methanol that have been intensively studied in the past in DFCs [19]. A very important fact is that secondary alcohols do not induce the formation

of CO that deactivates the catalyst material. However, in common proton exchange membrane fuel cells (PEMFCs), liquid isopropanol and acetone gradually dissolve the typically applied Nafion membrane over time, which leads to fuel crossover and, thus, a reduction of power density and efficiency [20]. To circumvent this problem, water is usually added to the isopropanol/acetone system in excess [20–23]. By this, not only the fuel crossover is suppressed, but also the evaporation rate of isopropanol and acetone is reduced at the cost of lowered energy density in the storage medium [21–23]. Overall, the isopropanol/acetone LOHC system with its option for direct electrification of isopropanol is highly promising and technologically attractive for stationary and seasonal energy storage.

The design and operation of isopropanol DFCs requires knowledge about the thermophysical properties of the involved working fluids in form of diluted aqueous solutions of isopropanol and acetone. The present work focuses on the liquid density ρ_L, the liquid dynamic viscosity η_L, and the interfacial tension σ between the gas and liquid phase of the binary mixtures containing water and isopropanol or acetone. As will be shown throughout this work, there is a very scarce experimental data situation in the literature for the three mentioned properties of aqueous solutions of isopropanol or acetone at process-relevant conditions for the LOHC system. The latter conditions refer to temperatures T above 323 K and amount fractions of the solutes below 0.1. In this context, the term "amount fraction," which is often denoted by the synonym "mole fraction" in the literature, is the recommended term by the International Union of Pure and Applied Chemistry (IUPAC) [25] to define the number of entities of a constituent divided by the total number of entities in the mixture. One reason for this limited experimental database may be metrological challenges in the realization of experiments at elevated T under equilibrium conditions due to the relatively large vapor pressures of isopropanol and acetone. Considering the complex fluid structure of diluted aqueous solutions with alcohols or ketones, which can lead to the formation of microheterogeneities or clusters in the liquid phase [26–28], the necessity of realizing measurements on equilibrium properties and, in particular, on transport properties very close to equilibrium without applying macroscopic gradients or external forces is further emphasized. The complex fluid behavior of such aqueous solutions also poses challenges to accurately model their thermophysical and structural properties by using, for example, molecular simulation methods [29, 30].

The objective of the present study is the characterization of diluted aqueous solutions of isopropanol or acetone in a T range from (283 to 403) K at ambient pressure at or close to saturation conditions by the investigation of their thermophysical properties η_L, σ, and ρ_L. As model systems for the fully hydrogenated and dehydrogenated scenario in isopropanol DFCs, binary mixtures of water with isopropanol amount fractions of 0.02, 0.04, or 0.08 and with an acetone amount fraction of 0.04 have been studied at a pressure p of about 0.1 MPa. In addition, the influence of H_2 on η_L and σ of an aqueous solution with an isopropanol amount fraction of 0.04 at p up to 7.5 MPa was investigated as a model system that is not directly relevant within DFCs, yet representative for the prior hydrogenation step from acetone to isopropanol. Different light scattering techniques given by surface light scattering (SLS), dynamic light scattering (DLS) from bulk fluids with dispersed particles,

and polarization-difference Raman spectroscopy (PDRS) were used for contactless measurements at macroscopic thermodynamic equilibrium. For comparison and data evaluation purposes, also capillary viscometry (CV), the pendant-drop (PD) method, and vibrating-tube densimetry (VTD) were employed as conventional methods. The application of the aforementioned techniques for the accurate determination of the study-relevant thermophysical properties of fluids, including their mixture composition, has been demonstrated in recent studies on, for example, hydrocarbon-based LOHCs, see, e.g., Refs. [31–38]. To gain insight into the fluid structure and to interpret the experimental results, equilibrium molecular dynamics (EMD) simulations were additionally conducted for selected aqueous solutions of isopropanol or acetone.

2 Methods

In this section, a concise description of the experimental and simulation methods used in the present work is given. In addition to conventional methods, light scattering techniques exhibit the methods that are in the main focus. Furthermore, EMD simulations were employed to calculate the thermophysical properties and analyze the fluid structure.

2.1 Conventional Methods

2.1.1 Vibrating-Tube Densimetry (VTD)

The liquid density ρ_L was measured with a vibrating-tube densimeter DMA 5000 from Anton Paar. The measurement principle is based on the measurement of the natural frequency of a U-shaped glass tube filled with the liquid of interest. Using reference substances, the DMA 5000 was calibrated and afterward adjusted with air and deionized degassed water, as described in Ref. [32]. Before each experiment performed in this work, the validity of the calibration was checked by measuring deionized water and air.

2.1.2 Capillary Viscometry (CV)

In CV, the liquid kinematic viscosity ν_L is determined by measuring the flow time of the liquid through a capillary. By multiplying the flow time with the calibration constant of the capillary, ν_L is obtained. For this, Ubbelohde capillaries of the types 0, 0c, and 0a were used. Details on the calibration of types 0a and 0 can be found in Ref. [39] and on that for type 0c in Ref. [33]. For the accurate determination of ν_L, the Hagenbach correction accounting for acceleration effects within the flow through the capillary is additionally considered. A more detailed description of the principles of CV can be found in Refs. [40, 41].

2.1.3 Pendant-Drop (PD) Method

The gas–liquid interfacial tension σ was determined via the PD method. For this, the shape of an axisymmetric pendant drop hanging on the tip of a capillary is analyzed. The contour of the drop is influenced by the interplay of gravitational, buoyancy, and capillary forces, which is described by the Young–Laplace equation [42]. From the comparison of the experimentally recorded and the theoretical droplet shape via axisymmetric drop shape analysis (ADSA), σ can be obtained with the help of the knowledge of the densities of the liquid (ρ_L) and gas (ρ_G) phase. Further details on the theory behind this method and its data evaluation can be found in Refs. [42, 43].

2.2 Light Scattering Techniques

2.2.1 Surface Light Scattering (SLS)

Light scattering from surface waves, also known as surface light scattering (SLS), was used for the simultaneous determination of η_L and σ at vapor–liquid equilibrium (VLE). The method probes the dynamics of surface waves of a defined modulus of the wave or scattering vector q at the phase boundary between two fluid phases via the analysis of the scattered light modulated by these surface waves [44–46]. Using photon correlation spectroscopy (PCS), the resulting measurement signal is a time-dependent second-order correlation function (CF) of the scattered light intensity. For the systems investigated in this work, the measured CFs always showed an oscillatory behavior which can be represented by a damped oscillation reflecting the dynamics of the surface fluctuations, i.e., their mean life time τ_C and their propagation frequency ω_q. At T below 323 K, where the reduced capillary number Y was between 0.4 and 20, the rotational flow in the bulk of the fluid had to be considered in the representation of the CFs, as outlined in Ref. [47]. By solving the dispersion relation for hydrodynamic surface fluctuations without the presence of viscoelastic effects, D(η_L, η_G, ρ_L, ρ_G, σ, τ_C, ω_q, q), η_L and σ can be determined simultaneously. For this, data for ρ_L, ρ_G, and the dynamic viscosity of the gas phase η_G are required as an input. Further information on the principles of SLS [44–46, 48] and its application in thermophysical property research on, e.g., hydrocarbon-based LOHCs [31–36] can be found in the literature.

2.2.2 Dynamic Light Scattering (DLS) from Bulk Fluids with Dispersed Particles

In an analog manner as for SLS, light scattering can also be applied to the bulk of the fluid, often referred to as conventional DLS [46, 49, 50]. This represents an alternative option for the determination of η_L. By the addition of a small amount of seed particles to a liquid, the relaxation behavior of statistical fluctuations in the particle number density can be analyzed by the scattered light at a defined modulus of the scattering vector q [46, 49, 51–53]. For monodisperse particles, the corresponding CF is described by an exponential with the characteristic decay time τ_C which is related to the translational particle diffusion coefficient D_P. In the hydrodynamic

regime and for diluted dispersions with a particle volume fraction smaller than about 10^{-4}, the Stokes–Einstein equation [54] is valid and gives a relation between D_P and η_L. An important factor for the accurate determination of η_L is the knowledge of the hydrodynamic diameter d of the added spherical particles which has to be calibrated in advance in a fluid of known η_L [52, 53, 55].

2.2.3 Polarization-Difference Raman Spectroscopy (PDRS)

In addition to these two forms of DLS analyzing quasi-elastic scattering processes, Raman spectroscopy (RS) was applied to study fluid composition and structure by analyzing inelastically scattered light. In the required calibration procedure, binary mixtures of known composition are studied, where characteristic vibrational Raman modes associated with the two molecular species are correlated with the amount fractions according to the procedure proposed in Ref. [56]. The calibration factor determined from this approach can then be used to evaluate the actual composition from the recorded Raman spectra of samples studied by other techniques, such as SLS and CV in this work. Here, polarization-difference Raman Spectroscopy (PDRS) detailed in Refs. [37, 57, 58] is used because this special form has shown to enhance the signal quality by minimizing fluorescent background.

2.3 Equilibrium Molecular Dynamics (EMD) Simulations

Complementary to the experimental methods, EMD simulations were conducted to calculate thermophysical and structural properties. Based on a reliable all-atom force field (FF) that defines the intra- and intermolecular interactions, Newton's equations of motion are solved at discretized time steps. From the dynamics of an ensemble of molecules, not only static properties such as ρ_L and σ, but also dynamic properties like η_L can be computed at equilibrium conditions. The theory behind EMD simulations and their evaluation for calculating different thermophysical properties including ρ_L, σ, and η_L can be found in, e.g., Refs. [59, 60].

3 Experimental and Simulation Details

3.1 Materials and Sample Preparation

The specifications of the liquids and gases used for the experiments are listed in Table 1. With the exception of water (H_2O), the purity of the liquid samples 2-propanone (C_3H_6O) and 2-propanol (C_3H_8O), also known as acetone and isopropanol, is given by the certificate of analysis from the supplier. The latter two liquids were also analyzed by gas chromatography coupled with flame-ionization detection (GC-FID) with regard to impurities. For the gases hydrogen (H_2) and helium (He), the purity is given by the amount fraction y, as specified by the suppliers. Besides the purities, also the molar mass M as well as the normal boiling point at 0.1 MPa, T_b, and the critical temperature T_c are given in Table 1. All binary mixtures of water

Table 1 Specification of the used chemicals

Sample	CAS number	Source	M/(g·mol^{-1})	T_b/K	T_c/K	Specified purity
Isopropanol	67-63-0	Merck	60.095	355.5	508.3	≥0.999[a]
Acetone	67-64-1	Merck	58.079	329.22	508.1	≥0.995[a,b] ≥0.999[a,c]
Hydrogen	1333-74-0	Air Liquide	2.016	–	33.15	$y \geq 0.999999$
Helium	7440-59-7	Air Liquide	4.0026	–	5.1953	$y \geq 0.99996$

[a]Purity as specified in the certificate of analysis provided by the supplier based on peak areas from GC-FID

[b]Sample used in SLS, DLS, and CV measurements

[c]Sample used in PDRS measurements

with isopropanol or acetone were prepared by a weighing procedure using an analytical balance (ENTRIS224I-1S, Sartorius) with 0.1 mg precision. The final mixture compositions are provided in the respective data tables in the manuscript and the Supplementary Information. During calibration measurements on the aqueous solutions by PDRS, small changes in composition over time were noticed. Thus, the samples were prepared and immediately filled in corresponding sample cells to minimize changes in composition due to evaporation effects. This aspect will be discussed in more detail in Sect. 4.1.

3.2 Experimental Procedure and Data Evaluation

3.2.1 Vibrating-Tube Densimetry (VTD)

ρ_L of the aqueous solutions was measured under ambient atmosphere at $p \approx 0.1$ MPa by VTD at T from (283.15 or 293.15) K up to a T that is slightly higher than the respective boiling point of isopropanol or acetone. To reduce evaporation effects, the inlet and outlet channel of the tube filled with the sample was connected to a syringe and a thin 10 cm long hose containing further liquid sample. All densities measured for water-isopropanol mixtures up to 358.15 K and for water–acetone mixtures up to 333.15 K agreed with the results of independent repetition measurements. The final data for ρ_L are the averages of the results obtained from two fillings of the DMA 5000, excluding unreliable measurements that showed bubble formation. All results are associated with expanded (coverage factor $k=2$) uncertainties of $U_r(\rho_L)=0.0002$ and $U(T)=0.01$ K.

3.2.2 Capillary Viscometry (CV)

With CV, ν_L was determined under ambient atmosphere at $p \approx 0.1$ MPa for water-isopropanol mixtures in a T range from (283 to 353) K and for water–acetone mixtures from (283 to 333) K. The Ubbelohde viscometers of types 0, 0c, and 0a were placed in a thermostatted water bath, as described in Ref. [61]. Close to the capillary, a Pt-100 Ω resistance probe calibrated with an uncertainty ($k=2$) of $U(T)=40$

mK was placed close to the capillary to measure the actual T. The T stability during one run was below 35 mK, resulting in an overall estimated uncertainty $U(T) = 75$ mK. For each T, five individual run times were measured, showing a maximum deviation from the average run time of less than 0.13%. Between the different runs, the liquid sample was pulled up slowly by applying a small pressure difference in order to minimize evaporation effects. The average of the run times was used to calculate ν_L taking into consideration the capillary constant and the Hagenbach correction. Then, ν_L was converted to η_L based on the correlation of the densities ρ_L measured in this work according to Eq. 2. Considering the generally increasing deviations between the individually determined viscosity values with increasing T from different fillings, the uncertainty ($k = 2$) of η_L is estimated to vary linearly with respect to T from $U_r(\eta_L) = 0.01$ at 283 K to $U_r(\eta_L) = 0.045$ at 333 K or 353 K for the mixtures with acetone or isopropanol.

3.2.3 Pendant-Drop (PD) Method

In this work, the same PD setup as described in Ref. [62] was used to measure σ of the aqueous isopropanol or acetone solutions from 303 K up to (363 or 323) K at $p \approx 0.1$ MPa under a vapor-saturated He atmosphere. The optical system was calibrated using a reference sphere to convert from the pixel to the metric scale. Then, the bottom of the used stainless-steel cell was covered with about 10 mL of liquid sample, i.e., ca. 25% of the inner cell volume. This ensures a vapor atmosphere around the PDs close to saturation conditions, aiming at minimizing evaporation effects on the measurements. Before heating, the gas phase inside the cell was purged with He multiple times, while the capillary was flushed with liquid sample. T was recorded by a Pt-100 Ω resistance probe calibrated with an uncertainty ($k = 2$) of $U(T) = 20$ mK and is characterized by a stability during one experiment of less than 38 mK. Based on these two influences, the uncertainty ($k = 2$) in the T measurement is estimated to be $U(T) = 60$ mK. For each state point, five individual drops were studied after an equilibration time of about 10 min. For each droplet, fives pictures were recorded, evaluated, and averaged to determine σ. The final value for σ is calculated by averaging the results for all droplets analyzed. In accordance with Ref. [62], the measurement results can be specified with an expanded uncertainty ($k = 2$) of $U_r(\sigma) = 0.02$.

3.2.4 Surface Light Scattering (SLS)

In the present study, SLS was applied to investigate aqueous solutions of isopropanol or acetone without or with the presence of H_2 in a T range from (303 to 403) K. The experimental setup used for the determination of η_L and σ by SLS is described in Refs. [35, 63]. The used stainless-steel sample cell was filled with the liquid sample and then flushed with He multiple times to remove any air from the vapor phase. Afterward, the experiments were conducted at macroscopic thermodynamic equilibrium close to saturation conditions in closed systems. Two different sets of measurements were performed depending on the applied gas atmosphere. The three water-isopropanol mixtures and one water–acetone mixture were studied

in the presence of a He atmosphere at a partial He pressure of about 0.1 MPa. For the water-isopropanol mixture with $x_{iso} = 0.04$, the influence of pressurized H_2 was investigated at total p of (0.1, 2.5, 5.0, and 7.5) MPa for T of (303, 343, and 403) K. Here, p was measured by a pressure transmitter (PA-33X, Keller) with an uncertainty of 5 kPa. The sample cell is equipped with three Pt-100 Ω resistance probes calibrated with an uncertainty ($k = 2$) of $U(T) = 30$ mK [63]. During the experiments, a T stability of better than 100 mK and, in most cases, better than 20 mK could be realized. Therefore, an overall uncertainty in T of $U(T)$ ranging from (50 to 130) mK can be estimated, which can be linearly interpolated from low to high T.

For the frequency-doubled Nd:YVO_4 laser with a wavelength in vacuo of $\lambda_0 = 532$ nm, the incident beam power was limited to 40 mW. The scattered light was detected perpendicularly to the interface in transmission direction. For each state, six CFs at different q were recorded which was realized by changing the external angle of incidence from (3.0 to 3.6)°. To determine η_L and σ by solving the dispersion relation of surface fluctuations, information of σ_L, σ_V, and η_V are required. Data for ρ_L characterized with $U_r(\rho_L) = 0.0002$ are obtained from Eq. 2 which is based on the present density measurements up to (333.15 or 358.15) K and was extrapolated to T up to 403.15 K. ρ_L of the ternary mixture consisting of water, isopropanol, and H_2 at different p was approximated by that of the binary water-isopropanol mixture at 0.1 MPa since dissolved H_2 has a negligible influence on ρ_L of water according to Refs. [64, 65]. For ρ_V, Raoult's law in combination with the assumption of an ideal gas is applied, estimating an uncertainty ($k = 2$) of $U_r(\rho_V) = 0.05$. η_V is calculated by the Lucas model, as described in Ref. [66], with an estimated uncertainty ($k = 2$) of $U_r(\eta_V) = 0.1$. The expanded ($k = 2$) uncertainties of the η_L and σ values were estimated by error propagation schemes [67].

During the experiments, strong light scattering originating from the liquid phase was observed for all mixtures, especially above 323 K. This may be connected to the formation of nanoscopic clusters in the aqueous solutions, as shown for the same or similar alcohol and ketone solutes in Refs. [26, 27, 68, 69]. The agreement of the η_L and σ data from repetition measurements at 323 K after studying 403 K with the initial results at 323 K suggests thermal stability of all samples.

3.2.5 Dynamic Light Scattering (DLS) from Bulk Fluids with Dispersed Particles

For aqueous solutions of isopropanol or acetone, η_L was determined under atmospheric pressure at $p \approx 0.1$ MPa via the measurement of D_P of dispersed seed particles by DLS. The experimental setup and data evaluation scheme are detailed in Refs. [52, 53]. At first, the two kinds of practically spherical silica particles (from Merck KGaA) with diameters d of around (100 or 200) nm were dispersed in deionized water. The dispersions were sonicated for ca. 15 min and then filtered using syringe filters (from Corning) with a pore size of (200 or 450) nm to remove any particle aggregates. Although the final particle volume fractions of the dispersions cannot be fully traced due to the filtration procedure, they are in the order of 10^{-4} and below, i.e., close to infinite dilution. By mixing the aqueous dispersions with acetone or isopropanol, sample compositions of (x_{iso} or x_{ace}) ≈ 0.040 were adjusted. To calibrate d of the particles, the aqueous

particle-containing dispersions were firstly investigated at $T = 298.2$ K. Thereafter, DLS experiments were performed on the water-based dispersions containing acetone or isopropanol at $T = (293.2$ and $303.0)$ K. All samples were kept in glass cuvettes that were sealed at the top using parafilm to minimize sample evaporation. For the evaluation of the DLS experiments, the refractive indices of all dispersions at the laser wavelength λ_0 were additionally measured by an Abbe refractometer.

For each sample and T, at least three DLS experiments were performed at external incident angles of (70, 90, and 110)°, resulting in six individual CFs using two correlator types. Instead of a heterodyne detection scheme that is typically beneficial for studying particulate systems [52, 53], a homodyne detection scheme was applied in all DLS experiments. The use of the latter scheme was necessary since disturbances in the form of oscillations were often observed in the heterodyne CFs, which hinders their proper evaluation. T of the sample was measured with a Pt-100 Ω resistance probe calibrated with an uncertainty ($k = 2$) of $U(T) = 20$ mK and showed an average stability during the measurement series of 1.7 mK. Therefore, an estimated uncertainty $U(T) = 25$ mK can be estimated for all T. Using the determined D_P and the viscosity of water of $\eta_L = 1.002$ mPa·s at $T = 293.2$ K [70], d was calibrated to be (105 ± 3) nm and (224 ± 7) nm for the two particle types. The final values for η_L of the aqueous isopropanol or acetone solutions were determined in the same procedure as applied in our previous study [71]. For the expanded ($k = 2$) uncertainties of η_L, a value of $U_r(\eta_L) = 0.05$ is estimated that considers the uncertainty due to the calibration and the statistical uncertainty from the different measurements per state.

3.2.6 Polarization-Difference Raman Spectroscopy (PDRS)

PDRS was applied during all SLS experiments and partly before and after CV experiments to track possible changes in the liquid composition of the aqueous solutions. At each thermodynamic state studied in the calibration measurements and in the SLS setup, at least eight polarized and depolarized spectra were recorded in order to calculate the isotropic spectra according to the procedure detailed in Refs. [37, 72]. The calibration of the Raman spectra was performed by analyzing the isotropic Raman spectra of the aqueous solutions with defined x_{iso} of 0.02, 0.04, 0.08, and 0.10 filled in closed cuvettes at T of (293, 393, and 323) K. The optical arrangement of the setup used for calibration in 180° backscattering direction is further described in Refs. [38, 72]. A Pt-100 Ω resistance probe calibrated with an uncertainty of $U(T) = 20$ mK was placed in direct contact with the liquid sample to record T. During the calibration measurements, a T stability better than 2 mK was achieved, resulting in an estimated total uncertainty of $U(T) = 22$ mK. The calibration factor K determined from the calibration was transferred to analyze Raman spectra recorded before and after selected CV measurements within the same setup and within the SLS setup. For the latter, details on the realization of PDRS are given in Ref. [37].

3.3 EMD Simulation Details

Non-polarizable all-atom force fields (FFs) are employed for describing the pair-additive potential energy functions accounting for intra- and intermolecular interactions. Non-bonded interactions were modeled by the Lennard–Jones (LJ) 12−6 potential and the Coulombic potential within a cutoff radius of 1.6 nm. For water, the three-body SPC/E FF [73], neglecting the polarization term, was applied. For acetone and isopropanol, the FF parameters were taken from the Optimized Potentials for Liquid Simulations (OPLS) framework [74] using the 1.14*CM1A-LBCC charge model for neutral molecules [75–77]. To calculate LJ interactions between unlike atoms, geometric combination rules were applied [74, 78]. Intramolecular 1–4 LJ and electrostatic interactions were scaled by a factor of 0.5. All bonds were constrained using the linear constraint solver (LINCS) [79]. To control T and p, the Nosé−Hoover thermostat [80, 81] and the Parrinello−Rahman barostat [82, 83] with coupling times of (1 and 14) ps were used.

All EMD simulations were performed for binary mixtures of water with isopropanol or acetone at (x_{iso} or x_{ace}) ≈ (0.02 and 0.04) and T=(293.15, 323.15, 363.15, and 403.15) K using the GROMACS package, version 5.1.2 [78]. The equations of motion are solved at each time step of 2 fs using the leapfrog algorithm [60]. Periodic boundary conditions were applied in all directions. After randomly placing ca. 10,000 atoms in a cubic simulation box and conducting an energy minimization, the desired T and p were adjusted by a 1 ns run in the canonical (NVT) ensemble and a 9 ns run in the isothermal−isobaric (NpT) ensemble. For the systems in the slightly compressed liquid phase, where p was set 0.1 MPa above the saturation pressure, ρ_L was calculated from the last 8.5 ns of the NpT run, while a subsequent NVT run of around 65 ns enabled to calculate η_L based on the Green−Kubo method [84, 85]. In all these simulations, long-ranging LJ and electrostatic interactions beyond the cutoff were calculated using standard dispersion corrections [60] and particle mesh Ewald summation (PME) [86]. In a next step, the cubic simulation boxes were extended in z-direction by a factor of three to create a vapor–liquid equilibrium (VLE). Since an enrichment of the solute molecules at the vapor–liquid interface was observed, additional solute molecules were added to the simulation box to ensure the same liquid bulk composition as studied in the experiments. From the last 25 ns of the 30 ns NVT runs, not only density profiles across the interface were extracted, but also σ was calculated from the analysis of the pressure tensor [59, 60]. During the VLE simulations, the LJ-PME [87] and PME [86] algorithms were used to model long-ranging LJ and electrostatic interactions beyond the cutoff. All obtained values and their uncertainties are the averages and double standard deviations (k=2) of the results from three independent simulation runs.

4 Results and Discussion

4.1 Characterization of Composition and Fluid Structure by PDRS

For the calibration of PDRS, polarized and depolarized Raman spectra were recorded for aqueous solutions of isopropanol with the isopropanol amount fractions

x_{iso} of 0.020, 0.040, 0.080, and 0.100 at $T = (293, 303, \text{and } 313)$ K. Furthermore, one acetone–water solution with the acetone amount fraction x_{ace} of 0.040 was studied at $T = 303$ K as a testing set for the calibration. Since the cuvettes were carefully sealed and almost completely filled, the compositions of the binary mixtures are considered to be very close to the original ones prepared by the weighing procedure at room T.

Figure 1 shows two exemplary isotropic Raman spectra obtained for aqueous solutions of isopropanol or acetone with (x_{iso} or x_{ace}) ≈ 0.040 at about 303 K. The predominant Raman peak for water is represented by the O–H-stretching region that is located between around (3000 and 3700) cm^{-1} [88], see the region highlighted with the orange line in Fig. 1. In this region, also the contribution from the O–H group in isopropanol is present, yet relatively small because the amount fractions of isopropanol in the studied aqueous solutions were always below 0.10. While this additional signal contribution from its O–H group could be safely neglected here, it needs to be considered accordingly for calibration purposes at larger isopropanol contents. The characteristic Raman signature for isopropanol and acetone is reflected by the C–C-stretching mode at around (700 to 850) cm^{-1} [88, 89], see the region marked with green line and the inset figure in Fig. 1. In the case of isopropanol, the C–C-stretching mode is centered at around 820 cm^{-1} for both the pure substance and its aqueous solution. For acetone, however, the peak located at about 780 cm^{-1} [88] with respect to the pure liquid shows a blue shift toward larger wave numbers after the addition of water. This behavior seems to be related to changes in the fluid structure as a result of variations in the intermolecular interactions which influence the intramolecular C–C vibrations. While acetone molecules in the pure liquid self-associate mainly through dipole–dipole interactions, this self-association is disturbed in diluted aqueous solutions of acetone. Here, the polar ketone group in acetone interacts preferentially with water molecules [26]. Therefore, the C–C bond can vibrate more freely than for pure acetone, which leads to the blue shift. At the

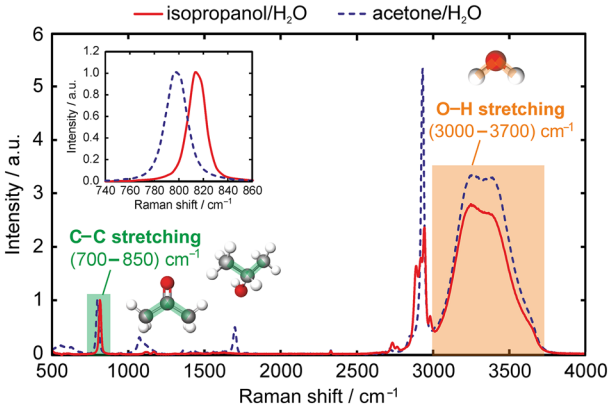

Fig. 1 Exemplary isotropic Raman spectra for aqueous solutions of isopropanol (solid red line) or acetone (dashed blue line) with (x_{iso} or x_{ace}) ≈ 0.040 recorded at 303 K. Selected Raman modes representative for isopropanol and acetone molecules (C–C stretching) as well as for water molecules (O–H stretching) are marked by the corresponding background (Color figure online)

same time, the C=O vibration at around 1700 cm^{-1} is red-shifted since the vibration of the carbonyl group is retarded by the surrounding water molecules. These findings are in agreement with results reported in literature for the same type of aqueous solutions [26, 89–91].

In the evaluation of the Raman spectra, the two peak areas related to the respective Raman modes, i.e., the intensity areas for the O–H stretching ($I_{O–H}$) and C–C stretching ($I_{C–C}$), were calculated to determine the intensity ratio $I_r = I_{O–H}/I_{C–C}$. The calculation of the peak areas and the further calibration procedure were conducted by a peak-fit algorithm as described in Ref. [88]. To represent the C–C-stretching areas for acetone and isopropanol, a Voigt profile was adjusted to the spectra data points. The O–H stretching region was modeled by three Gaussian functions with their peak centers between (3250 and 3760) cm^{-1}. To determine the calibration factor K, the defined compositions x_{iso} of all five studied water-isopropanol mixtures were fitted as a function of the corresponding I_r data determined from the isotropic spectra at all T according to [56]

$$x_{iso} = \frac{1}{1 + K \cdot I_r}. \tag{1}$$

The results from the calibration are listed in Table S1 of the Supplementary Information and are shown in Fig. 2. Here, the fit based on Eq. (1) can represent the measured intensity ratios reasonably well mostly within their calculated expanded ($k = 2$) uncertainties which are listed in Table S1 and not shown in Fig. 2. The average absolute relative deviation (AARD) of the amount fractions of the prepared samples given in Fig. 2 from the ones obtained by the calibration via Eq. 1 is 5.7%. This good agreement documents that the determined calibration constant $K = 0.424 \pm 0.012$ ($k = 2$) is T-independent for the limited T range between (293 and 313) K studied here. Equation (1) and the calibrated value for K were also applied at larger T because a calibration at T above 313 K may have been affected more strongly by evaporation effects during the measurements.

Although the calibration was performed based on aqueous solutions of isopropanol, it can be transferred to aqueous solutions of acetone. This could be confirmed exemplarily for an aqueous solution of acetone with $x_{ace} \approx 0.040$ at 303 K based on the sound agreement of the amount fraction determined by PDRS using Eq. (1) and

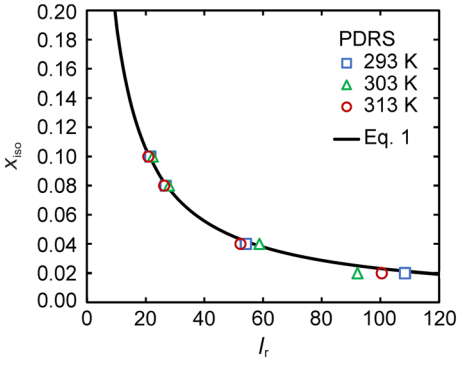

Fig. 2 Calibration results for PDRS showing x_{iso} as a function of the intensity ratio I_r obtained from the isotropic Raman spectra of aqueous solution of isopropanol at three different temperatures

K with that known from the mixing procedure. In addition, the Raman calibration could also be used to determine the composition of the liquid phase during SLS experiments. Here, the AARD between the Raman-determined and known amount fractions of all binary mixtures of water with isopropanol or acetone studied at 303 K and 323 K was 9.9%. The somewhat larger deviation is also caused by the comparatively weaker Raman signals detected under a scattering angle of 90° within the SLS setup. Thus, changes in composition during SLS experiments at different *T* up to 403 K could not be resolved quantitatively. Nevertheless, the PDRS measurements indicated no significant changes in the composition of the studied aqueous solutions over the investigated *T* range.

Considering all these findings, the solute amount fractions reported for all aqueous solutions that were investigated by the different experimental techniques refer to the originally prepared compositions and are associated with a conservative estimation of the relative uncertainty $U_r(x_{iso}) = U_r(x_{ace}) = 0.10$. This total uncertainty considers uncertainties introduced by the sample purities, the mixing procedure, and evaporation effects. Although the latter are presumably stronger at larger *T* and for open measurement systems like VTD and CV, it is too speculative to quantify the composition and its uncertainty for each technique and thermodynamic state.

4.2 Liquid Density

The experimental and simulation results for ρ_L of the studied binary mixtures at $p \approx 0.1$ MPa are listed in Tables S2 and S3. For each mixture, the measured data sets were correlated as a function of *T* with a third-order polynomial given by

$$\rho_{L,calc}(T) = \rho_0 + \rho_1 T + \rho_2 T^2 + \rho_3 T^3. \quad (2)$$

In the least-squares minimization algorithm, all data were considered with the same statistical weight. Table 2 summarizes the fit coefficients of Eq. 2 and the AARD values which are always clearly smaller than the relative experimental uncertainty ($k = 2$) with $U_r(\rho_L) = 0.0002$.

The measured and simulated densities of the binary aqueous solutions are illustrated together with reference data for pure water [92] recommended by the REFPROP database [93] and selected experimental data from literature [93, 95] as a function of *T* in Fig. 3. The experimental data from this work show the expected trend of decreasing ρ_L with increasing *T*. Compared to pure water, ρ_L increasingly decreases with increasing amount fraction of isopropanol or by the addition of acetone. This behavior can be related to the distinctly lower saturated liquid densities of isopropanol ($\rho_L = 785.15$ kg·m^{-3} at 293.15 K [39]) and acetone ($\rho_L = 790.00$ kg·m^{-3} at 293.15 K [39]) than that of water ($\rho_L = 998.16$ kg·m^{-3} at 293.15 K [92]). For a given solute amount fraction of 0.04, the mixtures with acetone have a slightly larger density than the mixtures with isopropanol at the same temperatures, where the difference is about 2.1% on average from (293.15 to 333.15) K. The data for ρ_L calculated by EMD simulations agree reasonably well with the experimental data. At the lowest studied *T* of 293 K, the deviation of simulated ρ_L values from $\rho_{L,calc}$ is within 2.2% for water with $x_{iso} = 0.020$ or 0.040 and 1.1% for

Table 2 Fit coefficients of Eq. 2 for the calculation of the liquid density $\rho_{L,calc}$ of aqueous solutions of isopropanol or acetone based on VTD data measured under ambient atmosphere at $p \approx 0.1$ MPa and T between (293.15 and 358.15 or 283.15 and 333.15) K

Sample	ρ_0/(kg·m^{-3})	ρ_1/(kg·m^{-3}·K^{-1})	ρ_2/(kg·m^{-3}·K^{-2})	ρ_3/(kg·m^{-3}·K^{-3})	AARD[a]/%
$x_{iso}=0.020$[b]	258.036	6.5035	-1.8093×10^{-2}	1.5000×10^{-5}	0.001
$x_{iso}=0.040$[b]	262.739	6.5666	-1.8697×10^{-2}	1.5833×10^{-5}	0.001
$x_{iso}=0.080$[b]	802.414	2.0715	-6.5003×10^{-3}	4.5474×10^{-6}	0.001
$x_{ace}=0.040$[b]	414.847	5.3599	-1.5503×10^{-2}	1.3056×10^{-5}	0.0004

[a]Average absolute relative deviation of measured ρ_L data from their fit

[b]Estimated relative uncertainty of amount fractions in binary mixtures is $U_r(x_{iso})=U_r(x_{ace})=0.10$

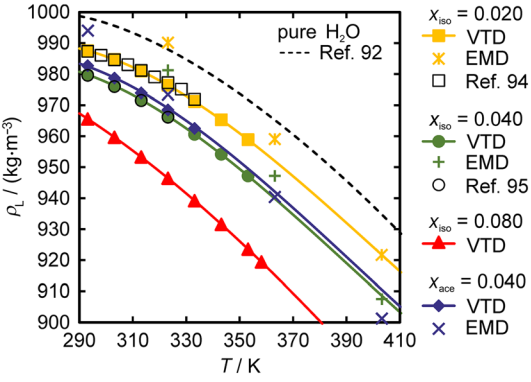

Fig. 3 Liquid density ρ_L of aqueous solutions of isopropanol or acetone at $p \approx 0.1$ MPa as a function of T obtained by VTD and EMD simulations from the present work. For comparison, the reference correlation for pure water [92] and the experimental data available in the literature [94, 95] for aqueous solutions of isopropanol at matching composition are included

water with $x_{ace}=0.040$. With increasing T, the deviations between the simulated data and the extrapolated fits based on Eq. 2 tend to decrease.

To the best of the authors' knowledge, there are currently no further experimental data available for the specific aqueous solutions with isopropanol or acetone studied in this work, except for the two data sets shown in Fig. 3. For aqueous solutions with isopropanol studied up to 333 K, the T-dependent data measured by Pang et al. [94] at $x_{iso}=0.020$ and by Zarei et al. [95] at $x_{iso}=0.040$ show AARDs from $\rho_{L,calc}$ of 0.04% and 0.03%, respectively. Although the relative deviations are slightly outside combined experimental uncertainties, good agreement between the values from literature and the present work is given.

The mixture behavior is further analyzed by the calculation of the molar excess volume V_m^E. It describes the difference between the actual molar volume of the mixture and the theoretical value calculated from a linear amount fraction-weighted mixing rule; see details in Ref. [38]. For the required densities of the pure components, the values for isopropanol and acetone were taken from Kerscher et al. [39] and those for water from the reference correlation [92]. To calculate the uncertainties of V_m^E, error propagation calculations in quadrature considering $U_r(\rho_L)=0.0002$ and $U_r(x_{iso})=U_r(x_{ace})=0.10$ were performed. The results in Fig. 4 show negative molar excess volumina for all mixtures, which is typical for aqueous solutions of alcohols [95] or ketones [96]. Although there is no T-dependent trend of the V_m^E data

within their uncertainties, the results for the aqueous solution at the largest isopropanol amount fraction of $x_{iso} = 0.080$ indicate decreasing V_m^E values at higher T. This behavior is in line with findings in the literature [95]. The increase in the magnitude of the V_m^E values with increasing x_{iso} appears to reflect the increasing strength of hydrogen bonding in mixtures of water and alcohols compared to that in the respective pure fluids [97]. Furthermore, the addition of isopropanol or acetone to water at a solute amount fraction of 0.040 results in very similar molar excess volumina.

4.3 Interfacial Tension

The experimental data for the interfacial tension σ measured by SLS and the PD method at around 0.1 MPa are given in Tables S4 and S5 of the Supplementary Information. Therein, also the EMD simulation results for σ are listed in Table S3. For comparison purposes, the SLS results were fitted as a function of T by a second-order polynomial function according to

$$\sigma_{calc} = \sigma_0 + \sigma_1 T + \sigma_2 T^2, \tag{3}$$

where all data points were considered with the same statistical weight within the least-squares minimization algorithm. The determined fit coefficients of Eq. 3 and the values for the AARD of the experimental data from the correlation are listed in Table 3.

4.3.1 Aqueous Solutions of Isopropanol

For aqueous solutions of isopropanol, the experimental and simulation results for σ from this work are shown as a function of T in Fig. 5. Here, the upper part illustrates the data in an absolute form, while the lower part depicts the deviation of these data from the SLS-based fit according to Eq. 3. For each system, σ_{calc} can represent the measured SLS data well within their uncertainties. The addition of isopropanol to water leads to a pronounced drop in σ, taking into consideration the recommended surface tension values of pure water [93] as upper boundary in the top part of Fig. 5.

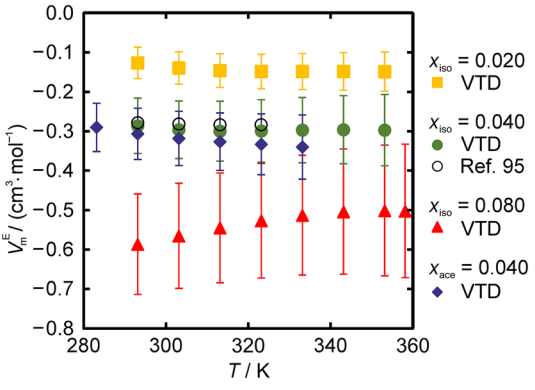

Fig. 4 Excess molar volume of aqueous solutions of isopropanol or acetone as a function of temperature at different compositions derived from the density measurements in this work and in Ref. [95]

Table 3 Fit coefficients of Eq. 3 for the calculation of the interfacial tension σ of aqueous solutions of isopropanol or acetone based on SLS data measured close to saturation conditions at $p \approx 0.1$ MPa and T between (303 and 403) K

Sample	σ_0/(mN·m^{-1})	σ_1/(mN·m^{-1}·K^{-1})	σ_2/(mN·m^{-1}·K^{-2})	AARD[a]/%
$x_{iso}=0.020$[b]	156.22	−0.59672	7.2534×10^{-4}	0.36
$x_{iso}=0.040$[b]	156.03	−0.64274	7.9736×10^{-4}	0.47
$x_{iso}=0.080$[b]	95.001	−0.34236	3.9525×10^{-4}	0.32
$x_{ace}=0.040$[b]	122.29	−0.34051	2.8564×10^{-4}	0.21

[a]Average absolute relative deviation of measured σ data from their fit

[b]Estimated relative uncertainty of amount fractions in binary mixtures is $U_r(x_{iso})=U_r(x_{ace})=0.10$

Compared to σ of H_2O ($\sigma=71.19$ mN·m^{-1} at 303.15 K), the interfacial tension at $x_{iso}=0.020$ ($\sigma=42.15$ mN·m^{-1} at 303.14 K) is already 41% lower and, thus, closer to the value of pure isopropanol ($\sigma=20.12$ mN·m^{-1} at 303.15 K [39]) for which the corresponding SLS data and fit correlation reported in Ref. [39] are also shown in Fig. 5.

The T-dependent decrease of σ of all three aqueous solutions from SLS becomes weaker with increasing T, which is also reflected by the PD data determined for $x_{iso}=0.040$. The low AARD of 1.3% of the PD values from σ_{calc} based on the SLS data indicates a very good agreement between the results from the two measurement techniques. It appears that a decrease of the isopropanol amount fraction in the liquid phase and within the vapor–liquid interfacial region due to its more pronounced evaporation than that of water in the closed sample cell is responsible for

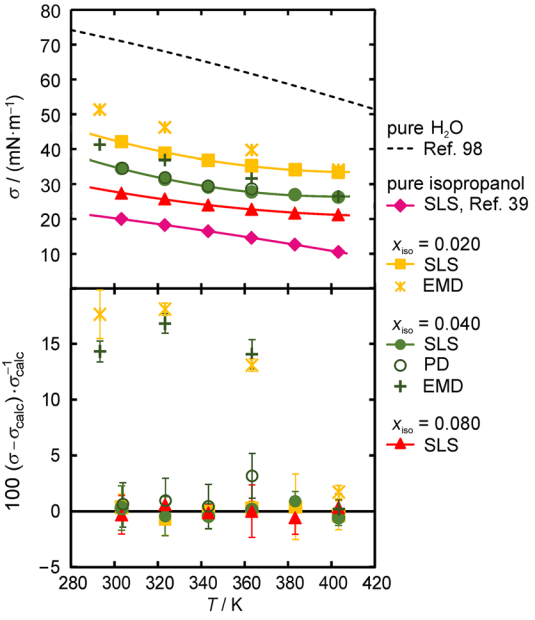

Fig. 5 Interfacial tension σ of aqueous solutions of isopropanol at $p \approx 0.1$ MPa as a function of T obtained by SLS, the PD method, and EMD simulations (upper part) and their relative percentage deviations from σ_{calc} (lower part). For comparison, the reference correlation for pure water [98] and the SLS data for pure isopropanol [39] are included in the upper part

the T-dependent trend. This issue will be discussed in more detail in Sect. 4.5 with the help of EMD simulations. The latter yield interfacial tensions which are at most 18% larger than the SLS data at 323 K, yet converge toward σ_{calc} at 403 K, as can be seen in the lower part of Fig. 5. The reason for this overestimation of σ is in accordance with overestimations of ρ_L and may be related to the underlying FF for water being the major component in the mixtures. Furthermore, σ is also very sensitive to the composition in the interfacial region which is dominated by the surface-active species isopropanol and acetone in mixtures with water. Minor differences in this composition between simulations and experiments may result in corresponding differences in the interfacial tension data.

A direct data comparison with measurements reported in the literature is not possible since different compositions of aqueous solutions of isopropanol were investigated compared to the present work. At least, two studies are available which focus on σ in the range of small isopropanol contents with $x_{iso} \leq 0.10$ at matching T. These are the work of Vazquez et al. [99] employing the Wilhelmy plate method and that of Hoke et al. [101] using the maximum bubble pressure method. In both studies, information about the uncertainty of σ and x_{iso} is lacking. The representation of these results, together with the SLS and PD results, at temperatures of (303 and 323) K as a function of x_{iso} in Fig. 6 shows that the two data sets from the literature match well and are generally larger than the present data. In comparison to the data from Vazquez et al. [99] that are connected by a polynomial fit as a guide for the eye in Fig. 6, the SLS results at 303 K deviate by − 7% at $x_{iso} = 0.020$ and − 3% at $x_{iso} = 0.080$. Since the measurements of Vazquez et al. [99] and Hoke et al. [100] were performed in open measurement systems, where the samples are in contact with air, evaporation of the low-boiling compounds from the liquid phase is likely, which may lead to changes in sample composition. As isopropanol is more volatile than water, which tends to cause smaller real x_{iso} values than those reported, systematically too large values for σ may be reasonable. At the same time, also the composition of the gas phase is probably different for open systems, where the gas

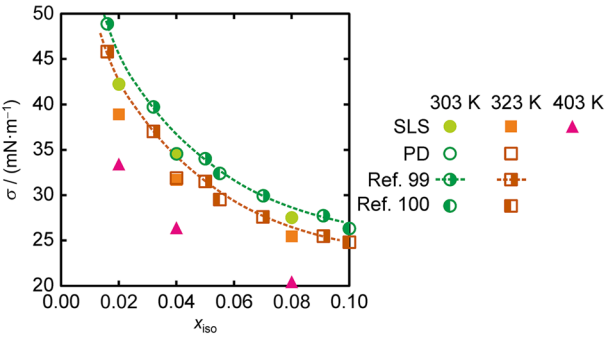

Fig. 6 Interfacial tension σ of aqueous solutions of isopropanol at $p \approx 0.1$ MPa at three selected temperatures as a function of x_{iso} obtained by SLS and the PD method in the present work in comparison to measurement results from Vazquez et al. [99] and Hoke et al. [100]. The data from Vazquez et al. are correlated as a function of x_{iso} by polynomial fits which are visualized by the dashed lines as a guide for the eye

atmosphere may not be fully saturated with vapor resulting in too large σ values in comparison to closed systems as present during SLS. In addition, evaporation may reduce T at the vapor–liquid interface of the fluid to a lower value than that associated with the reported data for σ. As a result, the interfacial tensions may be further overestimated at the reported T, considering the T-dependent behavior of σ. The aforementioned effects are excluded for the present PD and, in particular, SLS investigations because they were performed in closed measurement systems in thermodynamic equilibrium at or very close to saturation conditions.

4.3.2 Aqueous Solution of Acetone

For the aqueous solutions of acetone, the T-dependent results for σ of a representative mixture with $x_{ace} = 0.040$ determined by SLS, the PD method, and EMD simulations are shown in the upper part of Fig. 7 in comparison to reference data for pure acetone obtained by SLS [39] and for water [93]. Again, a significant reduction in σ is observed by adding acetone with $x_{ace} = 0.04$ to water. For 303 K, σ of the aqueous acetone solution is decreased by − 36% relative to the value for pure water. This decrease is smaller than observed for the aqueous isopropanol solution with –51% at the same solute amount fraction of 0.040. With increasing T, the difference between the two data sets at $x_{ace} = x_{iso} = 0.040$ decreases. This behavior indicates that isopropanol with an only slightly lower surface tension ($\sigma = 20.12$ mN·m^{-1} at 303.15 K [39]) than acetone ($\sigma = 21.61$ mN·m^{-1} at 303.15 K [39]) is more surface-active in mixtures with water.

Although the PD values agree again well with the SLS data, the deviations are larger than for the aqueous solutions with isopropanol. The deviation plot in the

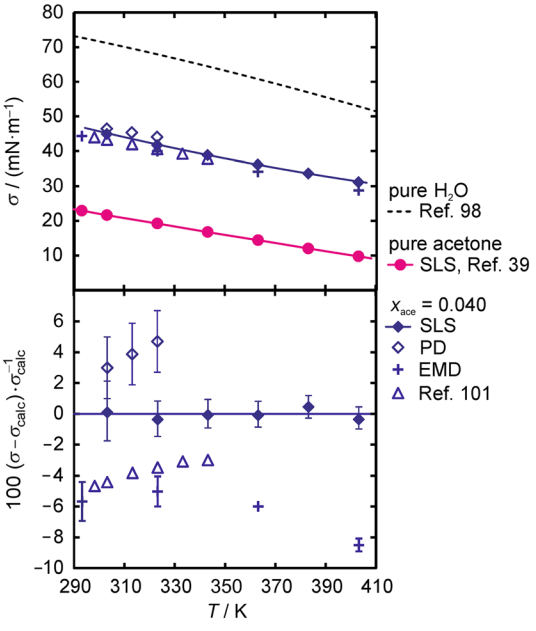

Fig. 7 Interfacial tension σ of an aqueous solution of acetone at $p \approx 0.1$ MPa as a function of T obtained by SLS, the PD method, and EMD simulations (upper part) and their relative percentage deviations from σ_{calc} (lower part). For comparison, the reference correlation for pure water [98], and the SLS data for pure acetone [39] are included in the upper part. Furthermore, the experimental data reported by Toryanik and Pogrebnyak [101] are shown in the upper and lower part

lower part of Fig. 7 shows that the PD results are systematically larger than σ_{calc} in a range between + 3.0% at 303 K and + 4.7% at 323 K, which is mostly outside combined uncertainties. The increasing deviations at larger T may point at a stronger evaporation of the highly volatile acetone from the liquid phase to the vapor phase during the PD measurements than during the SLS measurements. In the latter, about each half of the inner sample cell volume (~ 100 ml) was occupied by the liquid and the vapor phase, while the liquid-to-vapor ratio was about 1:3 in the sample cell for the PD measurements. Due to the different filling levels, the originally same liquid-phase compositions during the filling procedure tend to slightly change in the two measurement techniques, where x_{ace} in the PD experiments is likely to be somewhat lower than that in the SLS experiments, especially at larger T. This would result in larger σ values determined by the PD method and may also explain the behavior for the aqueous isopropanol solution in Fig. 5, where the largest deviation of the PD value from the SLS result of + 3% was observed at the largest T of 363 K.

The only available experimental data in the literature measured at practically the same composition with $x_{ace} = 0.0396$ and reported by Toryanik and Pogrebnyak [101] originate from the maximum bubble pressure method. Their results for σ determined up to 343 K are (5 to 3)% lower than the SLS results. A deeper discussion of this discrepancy is not possible due to missing information about the uncertainties of σ in the work of Toryanik and Pogrebnyak [101]. The EMD simulations at $x_{ace} = 0.04$ provide lower σ values compared to the SLS data, with deviation from − 5% at 323 K to − 8% at 403 K. This is opposite to the trend found for the analog solution with isopropanol, and might be mainly caused by minor differences in the surface structure and composition between simulations and experiments that cause variations in the macroscopic interfacial tension values.

4.4 Liquid Viscosity

The experimental data for η_L of the aqueous solutions determined by SLS close to 0.1 MPa are listed in Table S4 of the Supplementary Material. Moreover, the values for η_L at about 0.1 MPa measured by CV and DLS as well as those calculated by EMD simulations are found in Tables S6, S7, and S3, respectively. As a reference for data comparison over a broader T range, the T dependence of the SLS results was represented by a function according to

$$\eta_{L,calc} = \eta_0 \cdot \exp\left(\sum_{i=1}^{3} \eta_i \cdot T^{-i}\right). \tag{4}$$

In the least-squares fitting procedure, all experimental data points were displayed by $\ln(\eta_L / (\text{mPa·s}))$ as a function of T^{-1}/K^{-1} and were considered with the same statistical weight. The respective fit parameters of Eq. 4 and the AARD of the measured from the fit data are listed in Table 4. However, as explained later in this section, the SLS measurements of the viscosity for the aqueous solutions with isopropanol may be affected by a method-specific effect, which is why the fit parameters in Table 4 should be used with caution in these cases.

4.4.1 Aqueous Solutions of Isopropanol

The liquid viscosities of the three investigated aqueous isopropanol solutions at $x_{ace} = (0.020, 0.040, \text{and } 0.080)$ determined by SLS and correlated via Eq. 4 are illustrated as a function of T in the upper part of Fig. 8. In its lower part, also the measurement results from CV and DLS as well as the EMD simulation results are included next to the SLS results. In most of the cases, $\eta_{L,calc}$ can represent the experimental SLS data within their uncertainties. By adding small amounts of isopropanol to water, a strong increase in the mixture viscosity can be found, which is reasonable considering the larger η_L of isopropanol ($\eta_L = 1.78$ mPa·s at 303.15 K [39]) compared to that of water ($\eta_L = 0.797$ mPa·s at 303.15 K [70, 93]); see upper part of Fig. 8. At 303 K, for example, this percentage increase relative to η_L of water is 41%, 75%, and 131% for $x_{iso} = 0.020$, 0.040, and 0.080, respectively, while it becomes weaker with rising T. All aqueous solutions show the well-known behavior of liquids in the form of decreasing viscosities with increasing T.

The lower part of Fig. 8 shows that the data for η_L obtained by CV and DLS agree with each other within combined uncertainties and are systematically lower than $\eta_{L,calc}$ based on the SLS results. It should be mentioned that the fit based on Eq. 4 is an extrapolation at T below 303 K, which is why the data comparison with CV and DLS is less conclusive here. Independent of T, the absolute deviation between the SLS and CV data sets tends to increase with decreasing x_{iso}. For $x_{iso} = 0.020$, the maximum deviation of η_L from CV from $\eta_{L,calc}$ is –13% at 343 K. Lower viscosities from CV and DLS suggest that these measurement methods realized in sample cells open against ambient atmosphere may be affected by evaporation effects of the low-boiling isopropanol from the binary liquid mixtures. As discussed later in Sect. 4.4.2, exemplary CV measurements on aqueous solutions with the more volatile acetone indicate slight variations in sample composition and viscosity, especially after investigating larger T. However, these effects cannot be held entirely responsible for the observed discrepancies of the CV and DLS data from the SLS results. In accordance with a former study [102], it seems that a SLS-specific effect at the interface related to a viscoelastic behavior of surface-active molecules is present for the aqueous solutions of isopropanol. A more detailed discussion of this effect will be given in Sect. 4.5 by considering an analysis of the interface structure by EMD

Table 4 Fit coefficients of Eq. 4 for the calculation of the dynamic viscosity η_L of aqueous solutions of isopropanol or acetone based on SLS data measured close to saturation conditions at $p \approx 0.1$ MPa and T between (303 and 403) K

Sample	η_0/(mPa·s)	η_1/(K)	η_2/(K^2)	η_3/(K^3)	AARD[a]/%
$x_{iso} = 0.020$[b]	$1.66367 \cdot 10^{-2}$	732.574	$1.06947 \cdot 10^{5}$	$1.75365 \cdot 10^{7}$	0.08
$x_{iso} = 0.040$[b]	$1.68199 \cdot 10^{-6}$	$1.10811 \cdot 10^{4}$	$-3.78478 \cdot 10^{6}$	$5.08637 \cdot 10^{8}$	0.33
$x_{iso} = 0.080$[b]	$4.22774 \cdot 10^{24}$	$-5.97764 \cdot 10^{4}$	$2.00132 \cdot 10^{7}$	$-2.13647 \cdot 10^{9}$	1.87
$x_{ace} = 0.040$[b]	$3.697624 \cdot 10^{-2}$	594.640	$-1.06798 \cdot 10^{5}$	$7.07402 \cdot 10^{7}$	0.31

[a]Average absolute relative deviation of measured η_L data from their fit

[b]Estimated relative uncertainty of amount fractions in binary mixtures is $U_r(x_{iso}) = U_r(x_{ace}) = 0.10$

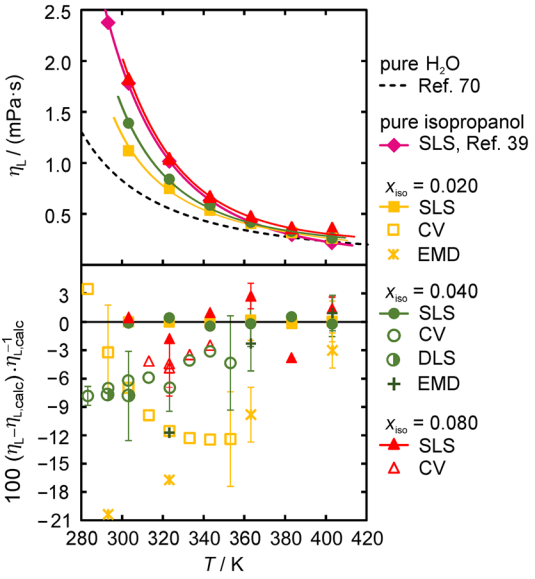

Fig. 8 Liquid viscosity η_L of aqueous solutions of isopropanol at $p \approx 0.1$ MPa as a function of T obtained by SLS (upper part) and the relative percentage deviations of the data obtained by SLS, CV, DLS, and EMD simulations from $\eta_{L,calc}$ (lower part). For comparison, the reference correlation for pure water [70] and the fit of the SLS data for pure isopropanol [39] are included in the upper part. In the lower part, the deviation of the MD value at 293.15 K and $x_{iso} \approx 0.04$ from $\eta_{L,calc}$ is not shown due to visibility purposes. Error bars are only shown exemplarily for the different data sets in the lower part

simulations. The latter yield predictions for η_L which agree very well with the experimental data sets within about a maximum deviation of –25% over the entire T range up to 403 K.

To the best of the authors' knowledge, there are no experimental studies available in the literature which focus on the same diluted compositions of aqueous isopropanol solutions as investigated in the present work. However, many studies such as that from Moha-Oucha et al. [103] examined aqueous solutions of isopropanol over the entire composition range and found a maximum in viscosity at x_{iso} of approximately 0.3. So far, only the study of Pang et al. [94] addressed η_L in the region of small $x_{iso} \leq 0.10$ at comparable T. Their data determined by CV are compared with the present SLS and CV results in Fig. 9, showing the dependency of η_L as a function of x_{iso} for three selected T of (303, 323, and 403) K. The relatively linear increase of the viscosity with increasing x_{iso} is visible at all three T, yet less pronounced at larger T. In comparison to the CV data from Pang et al. [94], which are fitted by a polynomial function as a guide for the eye in Fig. 9, our CV results agree well within $\pm 2\%$ over the studied composition range, while the SLS data are always larger with maximum deviations of $+13\%$ and $+6\%$ at $x_{iso} = 0.02$ and 0.04. At the largest amount fraction $x_{iso} = 0.08$, all three data sets match within 3% for (303 and 323) K.

4.4.2 Aqueous Solution of Acetone

The viscosity of an aqueous solution of acetone with $x_{ace} = 0.040$ was determined by SLS, CV, DLS, and EMD simulations, with the corresponding results shown as a function of T in Fig. 10. Its upper part depicts the measurement results in an absolute way, whereas the lower part provides their deviations from the SLS-based fit

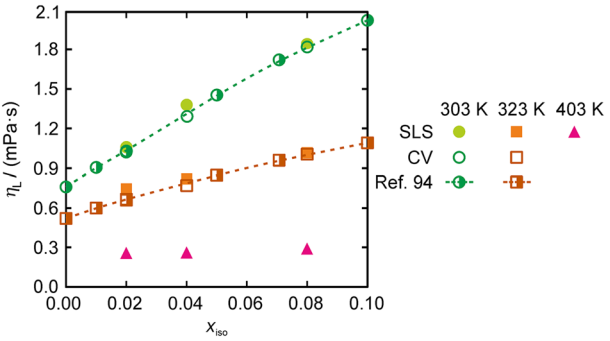

Fig. 9 Liquid viscosity η_L of aqueous solutions of isopropanol at $p \approx 0.1$ MPa at three selected temperatures as a function of x_{iso} obtained by SLS and CV in the present work in comparison to measurement results from Pang et al. [94]. The data from Pang et al. are correlated as a function of x_{iso} by polynomial fits which are visualized by the dashed lines as a guide for the eye

according to Eq. 4. For all T, the SLS data are represented by $\eta_{L,calc}$ well within their uncertainties. As can be seen from Fig. 10, η_L of the aqueous solution with $x_{ace} = 0.040$ is larger than the viscosities of both pure components. This behavior is remarkable because the saturated viscosity of acetone ($\eta_L = 0.300$ mPa·s at 303.15 K) [39] is significantly lower than that of water ($\eta_L = 0.797$ mPa·s at 303.15 K) [70, 93]. A CV-based comparison of the two aqueous solutions at a given solute amount fraction of 0.04 reveals that the mixture with acetone has only a slightly lower viscosity than that with isopropanol, amounting to about − 23% difference at 303.15 K. The main reason behind this strong viscosity increase for diluted acetone solutions is the intensification of the hydrogen bonding network in the water–acetone mixtures in comparison to that in pure water, as it was also discussed in the analysis of the PDRS experiments in Sect. 4.1. This network reaches its maximum strength at x_{ace} of around 0.1, i.e., in the range where also the viscosity shows the maximum value [26, 104]. At the same time, the hydrogen bonding between the O–H-group of water and the C=O group of acetone is accompanied by a hydrophobic assembly of the methyl groups of acetone molecules which leads to the formation of an ice-like structure [26]. With increasing T, the strengths of these intermolecular interactions and structures in the aqueous acetone solutions appear to weaken in a more pronounced way than in pure water since the values for η_L of the mixture and pure water tend to converge.

Since no experimental data for aqueous solutions with $x_{ace} = 0.040$ can be found in the literature, a comparison of the SLS results is only possible in relation to CV and DLS measurements. In line with the behavior for the aqueous isopropanol solutions, the η_L data for the acetone solutions measured by CV and DLS agree within combined uncertainties. These two data sets show good agreement with the SLS results since the relative deviations from $\eta_{L,calc}$ are within − 4%. These deviations are clearly smaller than those observed for the mixtures with isopropanol, although the latter compound is less volatile than acetone. To quantify anticipated evaporation effects during the CV experiments, two repetition measurements on solutions with

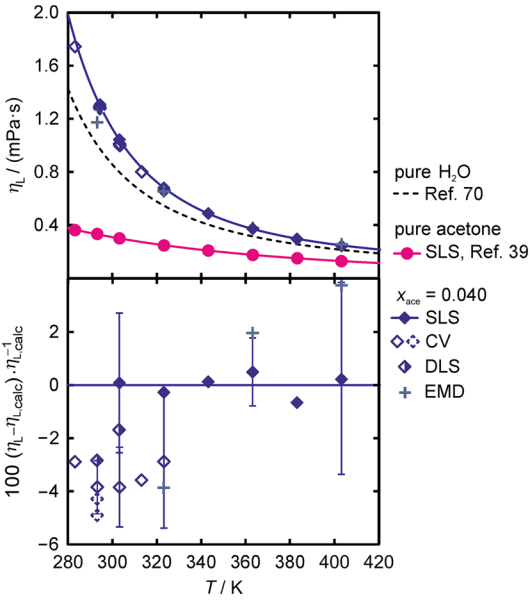

Fig. 10 Liquid viscosity η_L of an aqueous solution of acetone at $p \approx 0.1$ MPa as a function of T obtained by SLS, CV, DLS, and EMD simulations (upper part) and their relative percentage deviations from $\eta_{L,calc}$ (lower part). For comparison, the reference correlation for pure water [70] and the fit of the SLS data for pure acetone are included in the upper part. The two CV repetition measurements at 293 K are indicated by the symbols with the broken contour. In the lower part, the deviation of the EMD value at 293.15 K and $x_{ace} \approx 0.04$ from $\eta_{L,calc}$ is not shown due to visibility purposes. Error bars are only shown exemplarily for the different data sets

$x_{ace} \approx 0.040$ at 293 K after experiments at large T up to 353 K showed a stepwise decrease in η_L amounting to − 1.1% for the second repetition measurement relative to the original value; see the two data points with broken contour in Fig. 10. These findings are in accordance with additional PDRS measurements recorded before and after the CV experiments at 293 K that hint at a slight decrease of x_{ace} in the aqueous solution. Thus, the small differences between the SLS and CV or DLS data may mainly originate from small variations in the mixture composition. Again, the EMD results show very good agreement with the experimental data, with relative deviations from $\eta_{L,calc}$ between − 13% at 293 K and + 4% at 403 K.

In summary, the aqueous solutions of isopropanol are apparently adherent to a SLS-specific effect at the vapor–liquid interface that influences the dynamics of surface waves and leads to an overestimation of the apparent values for η_L. For the aqueous solution of acetone, the effect seems not to be present significantly, as deduced from the sound agreement between the SLS, DLS, and CV data for η_L. Since this effect is related to the presence of surface-active molecules, a more detailed analysis on the interface structure of the two different types of aqueous solutions is provided in the following section.

4.5 Structure of Vapor–Liquid Interfaces

To pinpoint possible effects from surface-active molecules on the SLS results, EMD simulations were performed for aqueous solutions of acetone or isopropanol at vapor–liquid equilibrium at four selected T of (293.15, 323.15, 363.15, and 403.15) K. Here, amount fractions of acetone and isopropanol in the liquid phase

of approximately 0.02 and 0.04 were adjusted. In Fig. 11, the partial number densities $\rho_{N,i}$ related to specific atoms i of the two solutes are shown as a function of the z coordinate of the simulation box, i.e., the axis perpendicular to the interface, for both aqueous solutions at the lowest and highest T of (293.15 and 403.15) K. The selected atoms are the oxygen (O) atom in the carbonyl (C=O) group of acetone and the hydrogen (H) atom in the hydroxyl (O–H) group of isopropanol as well as the carbon atom (C) in one of the two methyl groups of both compounds; see Fig. 11. By this selection of two terminal atoms in each molecule, it is easier to resolve the molecular orientation of the surface-active substances acetone and isopropanol in mixtures with water. It should be mentioned that the profiles $\rho_{N,i}$ depicted in Fig. 11 are averages of the profiles obtained around the two vapor–liquid interfaces present in the simulation box using the center of the liquid phase ($z = 0$) as a reference.

The results in Fig. 11 reveal that acetone (upper part) and isopropanol (lower part) are strongly enriched at the vapor–liquid interfaces. Using the C atoms as a reference, the enrichment factor defined as the ratio of the maximum partial density in the interfacial region to the mean partial density in the liquid phase is about 7.3 for acetone and 7.8 for isopropanol at 293 K. These similar surface activities for both solutes are in accordance with the comparable values for σ of the corresponding aqueous solutions. At larger T, the enrichment decreases in both cases and the profiles become broader. The same qualitative trends were also found for the mixtures with a solute amount fraction of 0.040. With respect to the orientation, clear differences between the two solutes can be observed. In the case of acetone, the profiles for O and C are overlapping and show no lateral displacement in z direction at both T. Therefore, it is plausible that for such a small molecule like acetone, a rather random orientation at the interface can be expected, which is already given at low

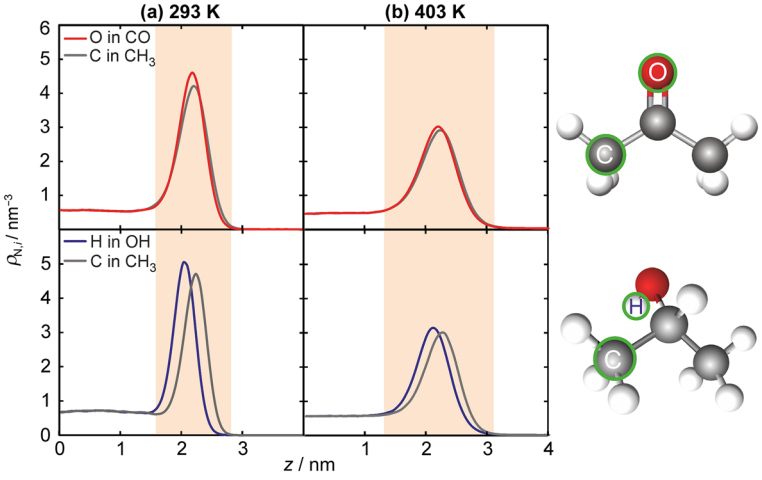

Fig. 11 Partial number density profiles $\rho_{N,i}$ for the atoms i in acetone (upper row) or isopropanol (lower row) as a function of the z coordinate of the simulation box evaluated from EMD simulations for aqueous solutions of acetone or isopropanol at $x_{ace} \approx 0.02$ or $x_{iso} \approx 0.02$ at (a) 293.15 K and (b) 403.15 K. The selected atoms in acetone and isopropanol are highlighted by green color in the displayed molecular structures. The interfacial regions are indicated by the shaded background (Color figure online)

T. In contrast, isopropanol shows a distinct orientation at the interface since the H atoms of the polar O–H group point toward the liquid phase, while the C atoms in one of the two nonpolar CH_3 groups are oriented toward the vapor phase. Such a configuration is energetically favorable considering the lower cohesive energy density of CH_3 groups than that of OH groups. The lateral distance between the maxima of the two peaks at 293 K (ca. 0.21 nm) tends to decrease slightly at higher *T* (ca. 0.14 nm). This indicates a small reorientation of isopropanol from a rather perpendicular orientation of the vector spanned between the selected H and C atoms with respect to the surface at low *T* toward a more parallel orientation at high *T*. All observations discussed for the solutions with x_{ace} or x_{iso} of 0.02 were qualitatively identical to those at a larger solute amount fraction of 0.04.

These results in the form of microscopic insights for the interface structure enable the interpretation of the behavior of the macroscopic properties. As detailed in Ref. [102], surface-active substances with a more or less pronounced molecular asymmetry may form a Gibbs monolayer at the interface of fluids and induce a viscoelastic behavior. The latter causes primarily an additional damping contribution to the dynamics of the surface fluctuations studied in the SLS experiment. In case the hydrodynamic theory neglecting such viscoelastic effects is applied, as valid in this work, this contribution causes apparent values for σ and η_L determined by SLS which are by trend smaller and larger than the actual values measured by conventional methods such as the PD method and CV [102]. Among the two studied types of aqueous solutions, such scenario is apparently only present for those of isopropanol, especially at low x_{iso} values, as discussed in connection with Figs. 5 and 8. In addition, the viscoelastic effects on the damping of surface waves tend to increase in strength when the surface-active molecules are oriented increasingly parallel to the interface, which may explain the larger discrepancies for η_L at larger *T* for low x_{iso}; see Fig. 8. With increasing x_{iso}, where the deviations of the SLS results from the data from conventional techniques decrease, it seems that the formation of a Gibbs monolayer is distorted, resulting in gradually decreasing viscoelastic effects.

In conclusion, the present SLS results for the aqueous solutions of isopropanol without and with H_2 represent apparent viscosity and interfacial tension values which need to be treated with caution. This could be considered by assigning an increased uncertainty of about 10% to the corresponding results for η_L and σ.

4.6 Influence of H_2 on Viscosity and Interfacial Tension of an Aqueous Solution of Isopropanol

To analyze the influence of H_2 on the liquid viscosity and interfacial tension of aqueous solutions, a mixture containing water with isopropanol at $x_{iso} = 0.040$ was investigated as a model system. The corresponding measurement results are listed in Table S8 of the Supplementary Information. Figure 12 illustrates the *p* dependence of the SLS results for σ and η_L in the presence of pressurized H_2 up to $p = 7.5$ MPa at $T = (303, 343, \text{and } 403)$ K in terms of their relative deviations from the reference values at the corresponding *T* and $p = 0.1$ MPa which are denoted by $\sigma_{0.1\ MPa}$ and $\eta_{L,0.1\ MPa}$. Since the total pressure *p* during the measurements was typically larger

than 0.1 MPa, especially at larger T due to the increasing vapor pressure of the solutions, the p-dependent values for σ and η_L were extrapolated to 0.1 MPa for each T to obtain $\sigma_{0.1\ MPa}$ and $\eta_{L,0.1\ MPa}$. This enables a better direct comparison of the different data sets. Although viscoelastic effects may also be present for aqueous isopropanol solutions saturated with dissolved H_2, the determined apparent values for σ and η_L allow for a reliable relative data comparison at different p and T in the following.

In the case of σ, dissolved H_2 shows a small yet resolvable influence which is partly outside combined uncertainties and depends on T. For $T = 303$ K, the relative deviations of σ from $\sigma_{0.1\ MPa}$ are negative and increase up to about 6% at $p = 7.5$ MPa. The latter state corresponds to a amount fraction of H_2 in the liquid phase, x_{H2}, of about 0.056, considering solubility data for H_2 in water [64, 65] and neglecting the presence of isopropanol. By increasing T, the relative deviations in σ decrease and are close to zero for the largest studied T of 403 K. Since x_{H2} tends to increase with increasing T for a given p, the relative deviations in σ for a given x_{H2} become smaller with increasing T. This is also in accordance with the trend that the generally weak enrichment of H_2 at vapor–liquid interfaces decreases with rising T [63].

With respect to η_L, most of the relative deviations of all measured data points up to $p = 7.5$ MPa from the corresponding reference values $\eta_{L,0.1\ MPa}$ are within combined experimental uncertainties and always within $\pm 3.2\%$, i.e., relatively small. The T-dependent behavior for η_L is in general very similar to that observed for σ. Reasons for this viscosity behavior are rather speculative, but are closely related to the interplay of the solvation effect due to dissolved H_2 and the compression effect

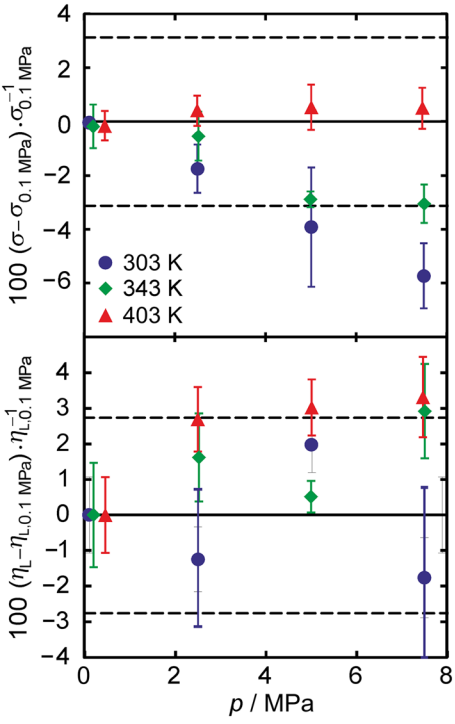

Fig. 12 Relative deviations of σ (upper part) and η_L (bottom part) of an aqueous solution of isopropanol with $x_{iso} = 0.04$ in the presence of a H_2 atmosphere from the extrapolated values at $p = 0.1$ MPa as a function of p measured by SLS. Error bars represent the experimental uncertainties ($k = 2$) of the measured data points and are only omitted for the σ and η_L values at $p \approx 0.1$ MPa and $T = 303$ K as well as for the η_L value at $p \approx 5.0$ MPa and $T = 303$ K due to the relatively large uncertainties up to $U_r(\eta_L) = 0.08$. The dashed lines indicate the average uncertainties of the measurement results at three different T obtained at the lowest p close to 0.1 MPa. These uncertainties are assigned for the reference values of $\sigma_{0.1\ MPa}$ and $\eta_{L,0.1\ MPa}$

due to pressure. While the former effect leads to a reduction of η_L, the latter one causes either a decrease or increase of η_L for pure water at small or high T [93].

Further experimental data for σ and η_L are not available for the specific aqueous solutions containing isopropanol and H_2 studied in this work. At least for mixtures of water with dissolved H_2, the interfacial tension was investigated in, e.g., Ref. [69], which reports the same qualitative trends on the influence of H_2 as observed here. Moreover, the H_2-induced variations in σ and η_L of the investigated aqueous solutions are very comparable to those found for other fluid classes including *n*-alkanes [105], alcohols [105, 106], bicyclic aliphatic and/or aromatic hydrocarbon-based LOHCs [62, 63], and ionic liquids [107].

5 Conclusions

The present study provides a comprehensive characterization of diluted aqueous solutions of isopropanol or acetone being part of a technically relevant hydrogen carrier system for applications in DFCs. For such complex systems with respect to their, e.g., relatively large volatility and sophisticated fluid structure, this work contributed to a reliable experimental database for ρ_L, η_L, and σ of solutions with solute amount fractions between 0.02 and 0.08 over a broad T range from (283 to 403) K, which represent process-relevant conditions in DFCs.

Although PDRS could not allow for a quantitative analysis of the changing mixture composition in the liquid phase during SLS measurements, it provided qualitative indications for a gradual decrease in the isopropanol or acetone amount fraction with increasing T as well as for pronounced hydrogen bonding interactions between unlike acetone and water molecules. This microscopic behavior seems to be responsible for the increasing negative excess molar volumina derived from the ρ_L results and for the strongly increasing η_L values with increasing x_{ace} or x_{iso}. With respect to σ, a significant reduction of up to about 60% at 303 K is observed by adding only small amounts of surface-enriching acetone or isopropanol to water, which is less pronounced for acetone than for isopropanol. Only for mixtures with the latter compound, it could be found with the help of EMD simulations that viscoelastic effects caused by a Gibbs monolayer at the interface are presumably responsible for discrepancies between σ and η_L values from SLS and the data from the PD method, CV, and DLS within about $\pm$ 10%. If such effects can be excluded, the application of SLS to such volatile fluid systems is highly predestinated due to its contactless working principle at macroscopic thermodynamic equilibrium. Further SLS experiments for an aqueous solution containing an isopropanol amount fraction of 0.04 showed that dissolved H_2 causes minor changes in σ and η_L for pressures up to 7.5 MPa.

In summary, the present experimental data for liquid density, liquid viscosity, and interfacial tension at or close to saturation conditions could significantly extend the so far relatively scarce data situation for diluted aqueous solutions of isopropanol or acetone, especially at large T. The reported thermophysical property data for the underlying binary subsystems can serve as a reference for future studies of ternary aqueous solutions with isopropanol and acetone, which represent solutions with varying compositions being present in direct isopropanol fuel cells.

Supplementary Information The online version contains supplementary material available at https://doi.org/10.1007/s10765-024-03449-6.

Acknowledgments The authors gratefully acknowledge funding of the Erlangen Graduate School in Advanced Optical Technologies by the Bavarian State Ministry for Science and Art. Furthermore, the authors thank Wenchang Wu for his support in the light scattering experiments from dispersed particles.

Author Contributions MK, JHJ, PW, and APF contributed to the study conception and design. Investigations by experiments and simulations and their evaluations were performed by JHJ, CHK, LMB, PKC, MK, and TK. The first draft of the manuscript was written by TMK. All authors reviewed the manuscript and approved the final version.

Funding Open Access funding enabled and organized by Projekt DEAL. This work was funded by the Bavarian Ministry of Economic Affairs, Regional Development and Energy.

Data Availability All data for the experimental and simulated thermophysical properties are available in the Supplementary Information.

Declarations

Conflict of interest The authors declare no competing interests.

References

1. B.A. Santasalo, T. Kallio, K. Kontturi, Platin. Met. Rev. **53**, 58 (2009). https://doi.org/10.1595/147106709X416040
2. T.Q. Hua, R.K. Ahluwalia, J.-K. Peng, M. Kromer, S. Lasher, K. McKenney, K. Law, J. Sinha, Int. J. Hydrogen Energy **36**, 3037 (2011). https://doi.org/10.1016/j.ijhydene.2010.11.090
3. J. Zheng, X. Liu, P. Xu, P. Liu, Y. Zhao, J. Yang, Int. J. Hydrogen Energy **37**, 1048 (2012). https://doi.org/10.1016/j.ijhydene.2011.02.125
4. W. Peschka, C. Carpetis, Int. J. Hydrogen Energy **5**, 539 (1980). https://doi.org/10.1016/0360-3199(80)90061-0
5. S.A. Sherif, N. Zeytinoglu, T.N. Veziroglu, Int. J. Hydrogen Energy **7**, 683 (1997). https://doi.org/10.1016/S0360-3199(96)00201-7
6. M.P. Suh, H.J. Park, T.K. Prasad, D.-W. Lim, Chem. Rev. **2**, 782 (2012). https://doi.org/10.1021/cr200274s
7. K.-H. Chung, Energy **35**, 2235 (2010). https://doi.org/10.1016/j.energy.2010.02.010
8. G.E. Ioannatos, X.E. Verykios, Int. J. Hydrogen Energy **35**, 622 (2010). https://doi.org/10.1016/j.ijhydene.2009.11.029
9. P. Adametz, K. Müller, W. Arlt, Int. J. Energy Res. **40**, 1820 (2016). https://doi.org/10.1002/er.3563
10. P. Schmidt, V. Batteiger, A. Roth, W. Weindorf, T. Raksha, Chem. Ing. Tec. **90**, 127 (2018). https://doi.org/10.1002/cite.201700129

11. F.V. Vázquez, J. Koponen, V. Ruuskanen, C. Bajamundi, A. Kosonen, P. Simell, J. Ahola, C. Frilund, J. Elfving, M. Reinikainen, N. Heikkinen, J. Kauppinen, P. Piermartini, J. CO2 Util. **235**, 28 (2018)
12. P. Rao, M. Yoon, Energies **13**, 6040 (2020). https://doi.org/10.3390/en13226040
13. K. Müller, Chem. Ing. Tec. **91**, 383 (2019). https://doi.org/10.1002/cite.201800043
14. P. Preuster, A. Alekseev, P. Wasserscheid, Annu. Rev. Chem. Biomol. Eng. **7**, 445 (2017). https://doi.org/10.1146/annurev-chembioeng-060816-101334
15. D. Teichmann, W. Arlt, P. Wasserscheid, R. Freymann, Energy Environ. Sci. **4**, 2767 (2011). https://doi.org/10.1039/c1ee01454d
16. N. Brückner, K. Obesser, A. Bösmann, D. Teichmann, W. Arlt, J. Dungs, P. Wasserscheid, Chemsuschem **7**, 229 (2014). https://doi.org/10.1002/cssc.201300426
17. D. Zakgeym, T. Engl, Y. Mahayni, K. Müller, M. Wolf, P. Wasserscheid, Appl. Catal. A **639**, 118644 (2022). https://doi.org/10.1016/j.apcata.2022.118644
18. D. Geburtig, P. Preuster, A. Bösmann, K. Müller, P. Wasserscheid, Int. J. Hydrogen Energy **41**, 1010 (2015). https://doi.org/10.1016/j.ijhydene.2015.10.013
19. G. Sievi, D. Geburtig, T. Skeledzic, A. Bösmann, P. Preuster, O. Brummel, F. Waidhas, M.A. Montero, P. Khanipour, I. Katsounaros, J. Libuda, K. Mayrhofer, P. Wasserscheid, Energy Environ. Sci. **12**, 2305 (2019). https://doi.org/10.1039/c9ee01324e
20. S. Auffarth, W. Dafinger, J. Mehler, V. Ardizzon, P. Preuster, P. Wasserscheid, S. Thiele, J. Kerres, J. Mater. Chem. A **10**, 17208 (2022). https://doi.org/10.1039/D2TA03832C
21. K. Braun, M. Wolf, A. de Oliveira, P. Preuster, P. Wasserscheid, S. Thiele, L. Weiß, M. Wensing, Energ. Technol. **10**, 2200343 (2022). https://doi.org/10.1002/ente.202200343
22. M. Brodt, K. Müller, J. Kerres, I. Katsounaros, K. Mayrhofer, P. Preuster, P. Wasserscheid, S. Thiele, Energ. Technol. **9**, 2100164 (2021). https://doi.org/10.1002/ente.202100164
23. P. Hauenstein, D. Seeberger, P. Wasserscheid, S. Thiele, Electrochem. Commun. **118**, 106786 (2020). https://doi.org/10.1016/j.elecom.2020.106786
24. M.C. Figueiredo, O. Sorsa, N. Doan, E. Pohjalainen, H. Hildebrand, P. Schmuki, B.P. Wilson, T. Kallio, J. Power. Sources **275**, 341 (2015). https://doi.org/10.1016/j.jpowsour.2014.11.034
25. IUPAC Compendium of Chemical Terminology, 3rd edition. International Union of Pure and Applied Chemistry; 2006. Online version 3.0.1 (2019). https://doi.org/10.1351/goldbook.A00296.
26. Z. Dou, L. Xing, W. Fang, C. Sun, Z. Men, Opt. Express **30**, 17270 (2022). https://doi.org/10.1364/OE.457580
27. H. Hayashi, K. Nishikawa, T. Iijima, J. Phys. Chem. **94**, 8334 (1990). https://doi.org/10.1021/j100384a062
28. A. Wakisaka, T. Ohki, Faraday Discuss. **129**, 231 (2005). https://doi.org/10.1039/B405391E
29. C. Zhang, X. Yang, Fluid Phase Equilib. **231**, 1 (2005). https://doi.org/10.1016/j.fluid.2005.03.018
30. A.D. Lavino, L. Banetta, P. Carbone, D.L. Marchisio, J. Phys. Chem. B **122**, 5234 (2018). https://doi.org/10.1021/acs.jpcb.8b01293
31. J.H. Jander, M. Kerscher, J. Cui, J. Wicklein, T. Rüde, P. Preuster, M.H. Rausch, P. Wasserscheid, T.M. Koller, A.P. Fröba, Int. J. Hydrogen Energy **47**, 22078 (2022). https://doi.org/10.1016/j.ijhydene.2022.04.275
32. M. Kerscher, J.H. Jander, J. Cui, M.M. Martin, M. Wolf, P. Preuster, M.H. Rausch, P. Wasserscheid, T.M. Koller, A.P. Fröba, Int. J. Hydrogen Energy **47**, 15789 (2022). https://doi.org/10.1016/j.ijhydene.2022.03.051
33. M. Kerscher, J.H. Jander, J. Cui, P. Wasserscheid, M.H. Rausch, T.M. Koller, A.P. Fröba, Int. J. Hydrogen Energy **48**, 29651 (2023). https://doi.org/10.1016/j.ijhydene.2023.04.103
34. M. Kerscher, J.H. Jander, J. Cui, L.A. Maurer, P. Wolf, J.D. Hofmann, A. Köksal, H. Zachskorn, F. Auer, P.S. Schulz, P. Wasserscheid, M.H. Rausch, T.M. Koller, A.P. Fröba, Int. J. Hydrogen Energy **77**, 1009 (2024). https://doi.org/10.1016/j.ijhydene.2024.06.131
35. M. Kerscher, T. Klein, P.S. Schulz, E. Veroutis, S. Dürr, P. Preuster, T.M. Koller, M.H. Rausch, I.G. Economou, P. Wasserscheid, A.P. Fröba, Int. J. Hydrogen Energy **45**, 2893 (2020). https://doi.org/10.1016/j.ijhydene.2020.07.261
36. P.S. Schmidt, M. Kerscher, T. Klein, J.H. Jander, F.E. Berger Bioucas, T. Rüde, S. Li, M. Stadelmaier, S. Hanyon, R.R. Fathalla, A. Bösmann, P. Preuster, P. Wasserscheid, T.M. Koller, M.H. Rausch, A.P. Fröba, Int. J. Hydrogen Energy **47**, 6111 (2022). https://doi.org/10.1016/j.ijhydene.2021.11.198
37. J.H. Jander, M. Kerscher, S. Li, M.H. Rausch, P. Wasserscheid, A.P. Fröba, Int. J. Hydrogen Energy **47**, 9331 (2022). https://doi.org/10.1016/j.ijhydene.2022.01.005

38. J.H. Jander, M.H. Rausch, P. Wasserscheid, A.P. Fröba, Int. J. Hydrogen Energy **78**, 1429 (2024). https://doi.org/10.1016/j.ijhydene.2024.06.357
39. M. Kerscher, L.M. Braun, J.H. Jander, M.H. Rausch, T.M. Koller, P. Wasserscheid, A.P. Fröba, Int. J. Thermophys. **45**, 8 (2024). https://doi.org/10.1007/s10765-023-03294-z
40. J. Millat, J.H. Dymond, W.A. Wakeham, *Transport Properties of Fluids: Their Correlation, Prediction and Estimation* (Cambridge University Press, Cambridge, 1996)
41. M.C.M. Sequeira, F.J.P. Caetano, J.M.N.A. Fareleira, Int. J. Thermophys. **45**, 118 (2024). https://doi.org/10.1007/s10765-024-03410-7
42. A.I. Rusanov, P.A. Prokhodrov, *Interfacial Tensiometry* (Elsevier, Amsterdam, 1996)
43. M.G. Cabezas, A. Bateni, J.M. Montanero, A.W. Neumann, Langmuir **22**, 10053 (2006). https://doi.org/10.1021/la061928t
44. A.P. Fröba, A. Leipertz, Int. J. Thermophys. **24**, 895 (2003). https://doi.org/10.1023/A:1025097311041
45. A.P. Fröba, S. Will, Light Scattering by Surface Waves—Surface Light Scattering, in *Experimental Thermodynamics, Vol. IX: Advances in Transport Properties of Fluids*. ed. by S. Will, Y. Nagasaka, A.P. Fröba, J. Winkelmann, S. Wiegand, W. Köhler (Royal Society of Chemistry, Cambridge, 2014), pp.19–35
46. T.M. Koller, M.H. Rausch, A.P. Fröba, Int. J. Thermophys. **45**, 57 (2024). https://doi.org/10.1007/s10765-024-03344-0
47. T.M. Koller, M. Kerscher, A.P. Fröba, J. Colloid Interface Sci. **626**, 899 (2022). https://doi.org/10.1016/j.jcis.2022.06.129
48. D. Langevin, *Light Scattering by Liquid Surfaces and Complementary Techniques* (Marcel Dekker, New York, 1992)
49. A. Leipertz, A.P. Fröba, Diffusion Measurements in Fluids by Dynamic Light Scattering, in *Diffusion in Condensed Matter—Methods, Materials, Models*. ed. by P. Heitjans, J. Kärger (Springer, Berlin, 2005), pp.581–620
50. A.P. Fröba, A. Leipertz, Diffusion measurements in fluids by dynamic light scattering. Diffus. Fundam. **2**, 1 (2005)
51. A. P. Fröba, Dynamic light scattering (DLS) for the characterization of working fluids in chemical and energy engineering. Habilitation thesis, Friedrich-Alexander-Universität Erlangen-Nürnberg (2009)
52. W. Wu, M.S.G. Knoll, C. Giraudet, M.H. Rausch, A.P. Fröba, Appl. Opt. **62**, 8007 (2023). https://doi.org/10.1364/AO.502659
53. W. Wu, J. Cui, U. Sultan, L. Gromotka, P. Malgaretti, C. Damm, J. Harting, N. Vogel, W. Peukert, A. Inayat, A.P. Fröba, J. Colloid Interface Sci. **641**, 251 (2023). https://doi.org/10.1016/j.jcis.2023.03.045
54. A. Einstein, Zeitschrift für Elektrochemie und Angewandte Physikalische Chemie **14**, 235 (1908). https://doi.org/10.1002/bbpc.19080141703
55. S. Bi, T.M. Koller, M.H. Rausch, P. Wasserscheid, A.P. Fröba, Ind. Eng. Chem. Res. **54**, 3071 (2015). https://doi.org/10.1021/acs.iecr.5b00086
56. S.K. Luther, J.J. Schuster, A. Leipertz, A. Braeuer, J. Supercrit. Fluids **84**, 146 (2013). https://doi.org/10.1016/j.supflu.2013.09.012
57. J. Kiefer, Anal. Chem. **89**, 5725 (2017). https://doi.org/10.1021/acs.analchem.7b01106
58. B. Auguié, A. Reigue, E.C. Le Ru, P.G. Etchegoin, Anal. Chem. **84**, 7938 (2012). https://doi.org/10.1021/ac301696p
59. D. Frenkel, B. Smit, *Understanding Molecular Simulation: From Algorithms to Applications* (Academic Press, San Diego, 2002)
60. M.P. Allen, D.J. Tildesley, *Computer Simulation of Liquids* (Oxford University Press, New York, 1987)
61. J. Cui, M. Kerscher, J.H. Jander, T. Rüde, P.S. Schulz, P. Wasserscheid, M.H. Rausch, T.M. Koller, A.P. Fröba, J. Chem. Eng. Data **67**, 3085 (2022). https://doi.org/10.1021/acs.jced.2c00519
62. J.H. Jander, P.S. Schmidt, C. Giraudet, P. Wasserscheid, M.H. Rausch, A.P. Fröba, Int. J. Hydrogen Energy **46**, 19446 (2021). https://doi.org/10.1016/j.ijhydene.2021.03.093
63. M. Kerscher, T. Klein, P. Preuster, P. Wasserscheid, T.M. Koller, M.H. Rausch, A.P. Fröba, Int. J. Hydrogen Energy **47**, 39163 (2022). https://doi.org/10.1016/j.ijhydene.2022.09.078
64. D. Li, C. Beyer, S. Bauer, Int. J. Hydrogen Energy **43**, 512 (2018). https://doi.org/10.1016/j.ijhydene.2017.07.228

65. S. Ansari, M. Safaei-Farouji, S. Atashrouz, A. Abedi, A. Hemmati-Sarapardeh, A. Mohaddespour, Int. J. Hydrogen Energy **47**, 37724 (2022). https://doi.org/10.1016/j.ijhydene.2022.08.288
66. B.E. Poling, J.M. Prausnitz, J.P. O'Connell, *The Properties of Gases and Liquids*, 5th edn. (McGraw-Hill, New York, 2001)
67. T.M. Koller, T. Klein, C. Giraudet, J. Chen, A. Kalantar, G.P. van der Laan, M.H. Rausch, A.P. Fröba, J. Chem. Eng. Data **62**, 3319 (2017). https://doi.org/10.1021/acs.jced.7b00363
68. D. Chandler, Nature **437**, 640 (2005). https://doi.org/10.1038/nature04162
69. J.G. Davis, K.P. Gierszal, P. Wang, D. Ben-Amotz, Nature **491**, 582 (2012). https://doi.org/10.1038/nature11570
70. M.L. Huber, R.A. Perkins, A. Laesecke, D.G. Friend, J.V. Sengers, M.J. Assael, I.N. Metaxa, E. Vogel, J. Phys. Chem. Ref. Data **38**, 101 (2009). https://doi.org/10.1063/1.3088050
71. W. Wu, M. Supper, M.H. Rausch, M. Kaspereit, A.P. Fröba, Int. J. Thermophys. **43**, 177 (2022). https://doi.org/10.1007/s10765-022-03101-1
72. J.H. Jander, M. Piszko, J.V.W. Kühl, M.H. Rausch, A.P. Fröba, J. Chem. Eng. Data **68**, 813 (2023). https://doi.org/10.1021/acs.jced.2c00727
73. H.J.C. Berendsen, J.R. Grigera, T.P. Straatsma, J. Phys. Chem. **91**, 6269 (1987). https://doi.org/10.1021/j100308a038
74. W.L. Jorgensen, S. Maxwell, R. Tirado-Rives, J. Am. Chem. Soc. **118**, 11225 (1996). https://doi.org/10.1021/ja9621760
75. L.S. Dodda, J.Z. Vilseck, J. Tirado-Rives, W.L. Jorgensen, J. Phys. Chem. B **121**, 3864 (2017). https://doi.org/10.1021/acs.jpcb.7b00272
76. L.S. Dodda, I. Cabeza de Vaca, J. Tirado-Rives, W.L. Jorgensen, Nucleic Acids Res. **45**, 331 (2017). https://doi.org/10.1093/nar/gkx312
77. W.L. Jorgensen, J. Tirado-Rives, Proc. Natl. Acad. Sci. (PNAS) **19**, 6665 (2005). https://doi.org/10.1073/pnas.0408037102
78. M.J. Abraham, T. Murtola, R. Schulz, S. Páll, J.C. Smith, B. Hess, E. Lindahl, SoftwareX **1–2**, 19 (2015). https://doi.org/10.1016/j.softx.2015.06.001
79. B. Hess, H. Bekker, H.J.C. Berendsen, J.G.E.M. Fraaije, J. Comput. Chem. **18**, 1463 (1997). https://doi.org/10.1002/(SICI)1096-987X(199709)18:12%3c1463:AID-JCC4%3e3.0.CO;2-H
80. W.G. Hoover, Phys. Rev. A **31**, 1695 (1985). https://doi.org/10.1103/PhysRevA.31.1695
81. S. Nosé, Mol. Phys. **52**, 255 (1984). https://doi.org/10.1080/00268978400101201
82. M. Parinello, A. Rahman, J. Appl. Phys. **52**, 7182 (1981). https://doi.org/10.1063/1.328693
83. S. Nosé, M.L. Klein, Mol. Phys. **50**, 1055 (1983). https://doi.org/10.1080/00268978300102851
84. M.S. Green, J. Chem. Phys. **22**, 398 (1954). https://doi.org/10.1063/1.1740082
85. R. Kubo, J. Phys. Soc. Jpn. **12**, 570 (1957). https://doi.org/10.1143/JPSJ.12.570
86. T. Darden, D. York, L. Pedersen, J. Chem. Phys. **98**, 10089 (1993). https://doi.org/10.1063/1.464397
87. C.L. Wennberg, T. Murtola, S. Páll, M.J. Abraham, B. Hess, E. Lindahl, J. Chem. Theory Comput. **11**, 5737 (2015). https://doi.org/10.1021/acs.jctc.5b00726
88. S.K. Luther, S. Stehle, K. Weihs, S. Will, A. Braeuer, Anal. Chem. **87**, 8165 (2015). https://doi.org/10.1021/acs.analchem.5b00699
89. T.B. Hunter, S.F. Rice, R.G. Hanush, Ind. Eng. Chem. Res. **35**, 3984 (1996). https://doi.org/10.1021/ie9505118
90. N. Wu, X. Li, S. Liu, M. Zhang, S. Ouyang, Appl. Sci. **9**, 1235 (2019). https://doi.org/10.3390/app9061235
91. P.G. Puranik, Proc. Indian Acad. Sci. Sect. A **37**, 499 (1953). https://doi.org/10.1007/BF03052670
92. W. Wagner, A. Pruß, J. Phys. Chem. Ref. Data **31**, 387 (2002). https://doi.org/10.1063/1.1461829
93. E. W. Lemmon, I. H. Bell, M. L. Huber, M. O. McLinden, NIST standard reference database 23: reference fluid thermodynamic and transport properties: National Institute of Standards and Technology, Standard Reference, version 10.0, Gaithersburg, United States (2018)
94. F.-M. Pang, C.-E. Seng, T.-T. Teng, M.H. Ibrahim, J. Mol. Liq. **136**, 71 (2007). https://doi.org/10.1016/j.molliq.2007.01.003
95. H.A. Zarei, S. Shahvarpour, J. Chem. Eng. Data **53**, 1660 (2008). https://doi.org/10.1021/je800158z
96. A. Estrada-Baltazar, A. de León-Rodríguez, K.R. Hall, M. Ramos-Estrada, G.A. Iglesias-Silva, J. Chem. Eng. Data **48**, 1425 (2003). https://doi.org/10.1021/je030102f
97. R. Palani, A. Geetha, Phys. Chem. Liq. **47**, 542 (2009). https://doi.org/10.1080/00319100802562862

98. International Association for the Properties of Water and Steam, IAPWS R1-76 (2014)
99. G. Vazquez, E. Alvarez, J.M. Navaza, J. Chem. Eng. Data **40**, 611 (1995). https://doi.org/10.1021/je00019a016
100. B.C. Hoke Jr., J.C. Chen, J. Chem. Eng. Data **36**, 322 (1991). https://doi.org/10.1021/je00003a019
101. A.I. Toryanik, V.G. Pogrebnyak, J. Struct. Chem. **17**, 464 (1977). https://doi.org/10.1007/BF00746671
102. T.M. Koller, M. Kerscher, A. Köksal, M.R. Stockerl, T. Klein, A.P. Fröba, J. Phys. Chem. B **127**, 10647 (2023). https://doi.org/10.1021/acs.jpcb.3c06309
103. M. Moha-Ouchane, C. Boned, A. Allal, M. Benseddik, Int. J. Thermophys. **19**, 161 (1998). https://doi.org/10.1023/A:1021455203728
104. Y.F. Chow, G.C. Maitland, J.M. Trusler, Fluid Phase Equilib. **475**, 37 (2018). https://doi.org/10.1016/j.fluid.2018.07.022
105. T. Klein, F.D. Lenahan, Z. Zhai, M. Kerscher, J.H. Jander, T.M. Koller, M.H. Rausch, A.P. Fröba, Int. J. Thermophys. **43**, 88 (2022). https://doi.org/10.1007/s10765-022-03012-1
106. M. Kerscher, J.H. Jander, F. Luther, P. Schühle, M. Richter, M.H. Rausch, A.P. Fröba, Int. J. Hydrogen Energy **48**, 26817 (2023). https://doi.org/10.1016/j.ijhydene.2023.03.312
107. Z. Zhai, G. Hantal, A. Cherian, A. Bergen, J. Chu, C.R. Wick, K. Meyer, A.-S. Smith, T.M. Koller, Int. J. Hydrogen Energy **72**, 1091 (2024). https://doi.org/10.1016/j.ijhydene.2024.05.249

Authors and Affiliations

Thomas M. Koller[1] · Julius H. Jander[1] · Chathura J. Kankanamge[1] · Lena M. Braun[1] · Pranay K. Chittem[1] · Manuel Kerscher[1] · Michael H. Rausch[1] · Tobias Klein[1] · Peter Wasserscheid[2,3,4] · Andreas P. Fröba[1]

✉ Andreas P. Fröba
andreas.p.froeba@fau.de

[1] Department of Chemical and Biological Engineering (CBI) and Erlangen Graduate School in Advanced Optical Technologies (SAOT), Institute of Advanced Optical Technologies – Thermophysical Properties (AOT-TP), Friedrich-Alexander-Universität Erlangen-Nürnberg (FAU), Paul-Gordan-Straße 8, 91052 Erlangen, Germany

[2] Helmholtz Institute Erlangen-Nürnberg for Renewable Energy (IEK-11), Forschungszentrum Jülich GmbH, Cauerstraße 1, 91058 Erlangen, Germany

[3] Department of Chemical and Biological Engineering (CBI), Institute of Chemical Reaction Engineering (CRT), Friedrich-Alexander-Universität Erlangen-Nürnberg (FAU), Egerlandstraße 3, 91058 Erlangen, Germany

[4] Institute for a Sustainable Hydrogen Economy, Forschungszentrum Jülich GmbH, Am Brainergy Park 4, 52428 Jülich, Germany